

Iron Responsive Element (IRE)-mediated responses to iron dyshomeostasis in Alzheimer's disease

Nhi Hin^{1,2}, Morgan Newman², Stephen Pederson¹, Michael Lardelli²

¹ Bioinformatics Hub, School of Biological Sciences, University of Adelaide

² Alzheimer's Disease Genetics Laboratory, School of Biological Sciences, University of Adelaide

Abstract

Background: Iron trafficking and accumulation has been associated with Alzheimer's disease (AD) pathogenesis. However, the role of iron dyshomeostasis in early disease stages is uncertain. Currently, gene expression changes indicative of iron dyshomeostasis are not well characterised, making it difficult to explore these in existing datasets.

Results: We identified sets of genes predicted to contain Iron Responsive Elements (IREs), and used these to explore iron dyshomeostasis responses in transcript datasets involving (1) cultured cells under iron overload and deficiency treatments, (2) post-mortem brain tissues from AD and other neuropathologies, (3) 5XFAD transgenic mice modelling AD pathologies, and (4) a zebrafish knock-in model of early-onset, familial AD (fAD). IRE gene sets were sufficiently sensitive to distinguish not only between iron overload and deficiency in cultured cells, but also between AD and other pathological brain conditions. Notably, we see changes in 3' IRE transcript abundance as amongst the earliest observable in zebrafish fAD-like brains and preceding other AD-typical pathologies such as inflammatory changes. Unexpectedly, while some 3' IRE transcripts show significantly increased stability under iron deficiency in line with current assumptions, many such transcripts instead show decreased stability, indicating that this is not a generalizable paradigm.

Conclusions: Our results reveal iron dyshomeostasis as a likely early driver of fAD and as able to distinguish AD from other brain pathologies. Our work demonstrates how differences in the stability of IRE-containing transcripts can be used to explore and compare iron dyshomeostasis responses in different species, tissues, and conditions.

Introduction

Alzheimer's Disease (AD) has evaded effective treatment for decades. With the failure of numerous recent amyloid beta-focused drug trials [1–4] it has become increasingly important to explore other factors contributing to the disease. Since the early days of AD research, iron trafficking and accumulation has been observed to be altered in AD [5–9]. Discoveries over the past decade suggest that disruptions to iron homeostasis drive feedback loops that result in further pathology in AD. Altered iron homeostasis has often been viewed under the lens of the amyloid hypothesis through its role in facilitating amyloid-mediated toxicity [10–14]. Central to the amyloid hypothesis was the finding that mutations in particular genes caused an early-onset familial form of AD (fAD), and this was explained by the ability of these mutations to alter production of the amyloid beta peptide in some way [15]. A recent hypothesis paper re-interpreted many of these studies without assuming a central role for amyloid and promoted an alternative idea of iron dyshomeostasis as a common unifying effect of mutations causing fAD [16]. Although not yet directly tested in fAD patients or in a fAD model, the hypothesis is consistent with the role of iron in many critical biological processes including cellular respiration, hypoxia, and immune responses, all of which are disrupted in AD. The ability of iron to cycle through its oxidation states is fundamental to its diverse biological functions, but can also result in oxidative damage to cells. This has led to the evolution of tightly regulated homeostatic mechanisms to control iron availability and

minimise toxicity (reviewed in [17]).

Currently, gene expression patterns representing responses to iron dyshomeostasis are not well-characterised. Cellular responses to iron dyshomeostasis are complex and involve several systems and layers of regulation. The stability of the transcription factor HIF1a, (a component of HIF1, a master regulator of responses to hypoxia) is regulated by an iron-dependent mechanism so that transcriptional responses to iron deficiency can resemble hypoxia responses [18]. However, cellular iron homeostasis is also regulated at the post-transcriptional level by the IRP/IRE system [19–21]. In this system, altered levels of available ferrous iron (Fe^{2+}) cause Iron Responsive Proteins (IRP1 or IRP2) to change conformation or stability respectively [22,23]. This alters their ability to bind cis-regulatory Iron Responsive Element (IRE) stem-loop motifs in the 3' or 5' untranslated regions (UTRs) of genes encoding products related to iron metabolism. Only a few IRE-containing genes have been characterised in detail, including TfR1 (transferrin receptor 1; 3' UTR IRE), DMT1 (divalent metal transporter 1; 3' UTR IRE), H- and L-ferritin (both 5' UTR IRE), and ferroportin (5' UTR IRE) [21]. In general, these well-characterised IRE-containing genes suggest that IRPs binding to 3' IREs tend to stabilise transcripts to increase protein translation, while binding to 5' IREs suppresses translation [20]. Currently however, global gene expression changes mediated by the IRP/IRE system have not been well-characterised, and the overall expression patterns of IRE-containing genes have not been explored in the context of AD. In addition, it is unclear how expression of these genes might differ between AD and other

neurodegenerative diseases, or how AD risk factors such as aging and hypoxia might contribute.

In this study, we utilised the SIREs (Searching for Iron Responsive Elements) tool [24] to predict and identify sets of IRE-containing genes in human, mouse, and zebrafish. We then applied these gene sets to explore overall IRP/IRE-mediated iron dyshomeostasis responses in datasets involving: (1) a cultured cell line subjected to iron overload and deficiency treatments, (2) a cohort of AD patients, healthy controls, and two other pathological conditions affecting the brain, (3) 5XFAD mice used to model the amyloid and tau pathology seen in AD, and (4) a zebrafish knock-in model possessing a fAD-like mutation.

Our IRE gene sets displayed significant enrichment in AD, the 5XFAD mouse model, and an fAD-like zebrafish model, demonstrating for the first time the early and extensive involvement of IRP/IRE-mediated iron dyshomeostasis responses in the context of AD. IRE gene sets were sufficiently sensitive to distinguish not only between iron overload and deficiency in a cultured cell line dataset, but also between AD and other pathological conditions affecting the brain (pathological aging and progressive supranuclear palsy), implying that the dysregulation of IRE-containing genes and iron dyshomeostasis responses in AD could differ from other conditions. Overall, our observations do not support the current assumption that IRP binding to 3' IREs generally stabilizes transcripts as both increases and decreases in abundance of transcripts with either 3' or 5' IREs were observed under most conditions.

Results

1. Defining sets of genes containing Iron Responsive Elements (IREs)

We utilised the SIREs (Searching for Iron Responsive Elements) tool, to define species-specific IRE gene sets by searching for IRE and IRE-like motifs in the 3' and 5' untranslated regions (UTRs) of the reference transcriptomes of human (hg38), mouse (mm10), and zebrafish (z11). SIREs assigns a quality-score to all detected IREs, with “high-quality” scores corresponding to canonical IREs and “medium-quality” or “low-quality” scores reflecting deviations from the canonical IRE (alternative nucleotide composition in the apical loop, one bulge at the 3' or one mismatch in the upper stem) that would still produce an IRE-like motif with the potential to be functional [24–28]. **Figure 1** summarises the IRP/IRE interaction effects on transcripts and gives examples of canonical and non-canonical IREs.

We defined four gene sets for each species as follows: **HQ 3' IREs** (high-quality predicted 3' IRE genes), **HQ 5' IREs** (high-quality predicted 5' IRE genes), **all 3' IREs** (including all low, medium, and high-quality predicted 3' IRE genes), and **all 5' IREs** (including all low, medium, and high-quality predicted 5' IRE genes). The size of these gene sets for each species and the overlap present is shown in **Figure 2** and the gene sets are provided in **Supplementary Table 1**. Overall, searching through human UTRs uncovered the largest number of predicted IRE genes, followed by mouse, and then zebrafish. Overlap between homologous genes from the IRE gene sets of different species was generally poor. The largest sets of genes shared between species were consistently found between human and mouse, which is reflective of their closer evolutionary divergence. While not

many high-quality IRE genes were identified across all three species, the few we identified are consistent with known and well-characterised IREs in the literature [29,30]. For example, the single shared **HQ 3' IRE** gene between the three species was *TFRC* (transferrin receptor), while the shared **HQ 5' IRE** genes between the three species included *FTH1* (ferritin heavy chain 1) and *ALAS2* (5'-aminolevulinatase synthase 2).

2. IRE gene sets are over-represented within up-regulated AD genes, but overall not well-represented in existing gene sets

We explored the biological relevance of the predicted IRE gene sets described above by testing whether genes within them were over-represented in existing MSigDB gene sets. We limited our analysis to gene sets from the following collections: Hallmark (non-redundant sets of ~200 genes each representing various biological activities), C2 (gene sets from databases including KEGG and Reactome and published studies), C3 (gene sets containing genes with motif elements), and C5 (gene sets based on gene ontology terms) (see **Methods**). We performed over-representation analysis for the predicted IRE gene sets (**all 3' IREs** and **all 5' IREs**) separately for each species (human, mouse, zebrafish), and used Wilkinson's meta-analytic approach to determine gene sets that were significantly over-represented across the three species' IRE gene sets. Our results indicated that 1,148 of 10,427 tested gene sets displayed over-representation of IRE gene sets across all three species (Bonferroni-adjusted Wilkinson's p -value < 0.05) (**Supplementary Table 2**). Remarkably, the “Blalock Alzheimer's Disease Up” gene set from the C2 collection was significantly over-represented in both the sets of **all 3' IREs** (Bonferroni-adjusted Wilkinson's p -value = $3.9e-14$) and **all 5' IREs** (Bonferroni-adjusted Wilkinson's p -value = $2.1e-26$) in the meta-analysis, and was also the gene set with the most significant over-representation of the human **all 3' IREs** set (Bonferroni-adjusted Fisher's exact test p -value = $7.8e-58$) (**Supplementary Table 2**). This supports that disturbance of iron homeostasis particularly distinguishes Alzheimer's disease from other disease conditions and pathways represented within the C2 collection. In addition, the top 15 MSigDB gene sets showing the most significant over-representation generally differed between species. However, in all cases, a large proportion of IRE genes from the predicted IRE gene sets were not contained within any of these top-ranked MSigDB gene sets or within the Heme Metabolism geneset belonging to the Hallmark collection (**Figure 3**). This demonstrates that the predicted IRE genes we defined are not fully captured by existing gene sets and so may be uniquely useful for investigating gene expression changes during the IRE-IRP response to iron dyshomeostasis.

3. Involvement of transcription factor regulation within IRE gene sets

To be confident that IRE gene sets accurately capture information about the IRP/IRE-mediated responses, we needed to investigate possible co-ordinate regulation by other factors. As a starting point, we examined whether known binding motifs for transcription factors were significantly over-represented in the promoter regions of genes within each IRE gene set (**all 3' IREs**, **all 5' IREs**, **HQ 3' IREs**, and **HQ 5' IREs**) for each species. We

detected significant over-representation of several transcription factors including the Klf14 motif in the zebrafish *all 3' IREs* set (FDR-adjusted p -value = 0.049), the E2F motif in the human *all 5' IREs* set (FDR-adjusted p -value = 0.049) and the Bach1 (FDR-adjusted p -value = 0.012), Nrf2 (FDR-adjusted p -value = 0.013), and NF-E2 (FDR-adjusted p -value = 0.019) motifs in the zebrafish *HQ 5' IREs* set (**Supplementary Table 3**). This suggests that the expression of subsets of genes in some of the IRE gene sets may be influenced by other factors.

4. Gene set enrichment testing approach

Our predicted IRE gene sets can be used in any standard gene set enrichment testing approach to detect potential changes in iron homeostasis between conditions. Our workflow, which we later successfully apply on human, mouse, and zebrafish datasets, is shown in **Figure 4**. Due to variability in the results produced by different gene set enrichment testing methods, we were inspired by the EGSEA framework [31] to combine the results from different methods. Based on an initial analysis using EGSEA, we chose *fry/mroast* [32,33], *camera* [34], and *fgsea* [35,36] as the representative methods to use. (See **Supplementary Figure 1** for a principal component analysis of results from different gene set enrichment analysis approaches.) A summary of the different characteristics of the three methods is shown in **Table 1**. The raw enrichment p -values from these approaches can be combined to obtain an overall enrichment p -value for each gene set. In accordance with EGSEA default parameters, we used Wilkinson's method to combine raw p -values, and then applied adjustment for multiple testing on all combined p -values. Along with performing this gene set enrichment testing on our IRE gene sets, we also recommend using the same method to test for enrichment for the MSigDB Hallmark gene sets as the diverse biological activities they represent help to provide context for interpreting the IRE enrichment results. To explore further the results of IRE gene set enrichment analysis, we use UpSet plots to display the overlap between sets of "leading-edge" genes in the *all 3' IREs* and *all 5' IREs* gene sets. The leading-edge genes can be interpreted as the core (often biologically important) genes of a gene set that account for the significant enrichment as calculated by GSEA [36].

5. Differences in IRE gene set enrichment during iron deficiency and iron overload in a cultured cell line

We first tested how our enrichment approach illuminated the effects of iron overload and deficiency in a cultured cell line microarray dataset from Caco-2 cells (GEO accession: GSE3573). As only one cell type contributed to this dataset, interpretation of the IRE enrichment results is simplified by not having to consider the differing iron requirements of different cell types. This allowed us to focus on whether the iron dyshomeostasis treatments (iron overload and iron deficiency) could be detected and distinguished in terms of their IRP/IRE system-driven transcript abundance response. Because the dataset was from a microarray experiment, we performed only the differential gene expression and gene set enrichment testing portions of our workflow. The results of Principal Component Analysis and differential gene expression analysis are provided in **Supplementary Figure 2**.

In general, we found iron deficiency and iron overload

treatments resulted in different gene expression responses. In terms of differential gene expression, iron deficiency was associated with 96 differentially expressed genes of which 10 possess predicted IREs while iron overload was associated with 212 differentially expressed genes (FDR-adjusted p -value from *limma* < 0.05) of which 33 possess predicted IREs (**Supplementary Figure 2**). There were 17 differentially expressed genes in common between iron deficiency and iron overload treatments, and all moved in opposite directions according to the treatment (i.e. increased abundance under iron deficiency and decreased abundance under iron overload, or vice versa). These differences between iron deficiency and iron overload were reflected in gene set enrichment analyses using the MSigDB Hallmark gene sets, where the gene sets involved and the proportions of gene transcripts with increased or decreased abundance differed (**Figure 5A**). As expected, IRE gene sets also showed significant enrichment under iron deficiency and overload conditions (**Figure 5B**) (Bonferroni adjusted p -value < 0.05).

We expected that iron deficiency would result in increased expression of genes with 3' IREs under the IRP/IRE paradigm. However, both the 3' and 5' IRE gene sets displayed mixed patterns of increased and decreased expression under both the iron deficiency and iron overload treatments (**Figure 5B**). This indicates it would be difficult to distinguish between these conditions based purely on the overall increases or decreases in the expression of IRE gene sets. Despite this, we see that the iron deficiency and iron overload treatments can be distinguished by their "leading-edge" genes (those genes contributing most to the enrichment signal for the predicted IRE gene sets (*all 3' IREs* and *all 5' IREs*)) (**Figure 5C**). This supports that gene set enrichment using our predicted IRE gene sets is sufficiently sensitive to detect whether iron dyshomeostasis is present and to distinguish between different IRE-mediated gene expression responses in iron deficiency and iron overload treatments.

6. A distinct iron homeostasis response in human AD patients compared to other neuropathologies

Given that IRE gene sets could distinguish between iron overload and deficiency in a cultured cell line, we next tested our gene sets on a more complex data set including cerebellum and temporal cortex tissue samples from post-mortem human brains. The brains originated from either healthy controls or patients with one of three conditions: AD; pathological aging (PA), a condition involving amyloid pathology but no significant dementia symptoms; or progressive supranuclear palsy (PSP), a tauopathy without amyloid pathology [37]. An important characteristic of the dataset is that both cerebellum and temporal cortex tissue samples were available from each patient. A summary of the 236 patients whose data we included in this analysis is shown in **Table 2** and the results of differential gene expression analysis and IRE gene set enrichment analysis are shown in **Table 3** and **Figure 6A**. In our analyses, we focus mainly on comparing conditions within each tissue rather than between tissues. This is because we found significant differences in the AD vs. control comparison in the temporal cortex compared to the cerebellum (see **Supplementary Figure 3**).

Overall, our IRE enrichment analyses indicate significant enrichment of IRE gene sets in all pathological conditions (AD, PA or PSP) compared to healthy controls within the cerebellum

and temporal cortex (**Figure 6A**). In all pathological conditions, 3' and 5' IRE gene transcripts show overall mixed patterns of abundance (e.g. increased and decreased). Further examination of the leading-edge genes from these IRE gene sets gives more insight regarding potential differences and similarities between AD, PA, and PSP (**Figure 6B**). Overall, AD, PSP, and PA appear to involve distinct yet partially overlapping IRE gene expression responses in a tissue-specific manner. Within the temporal cortex, there are 435 3' IRE leading-edge genes and 178 5' IRE leading-edge genes exclusively present in the "AD vs. control" comparison. These are greater numbers than for the other two conditions. Interestingly, AD and PA share only relatively small numbers of leading-edge genes despite the fact that many regard PA as a prodrome of AD [38]. These observations suggest that iron dyshomeostasis may be an essential component of AD cognitive change. Interestingly, in the cerebellum, while AD and PSP share many 3' and 5' IRE leading-edge genes, PA is associated with a large number of unique leading-edge 3' and 5' IRE genes, further emphasising its difference from AD and also PSP. In general, our IRE gene sets appear sufficiently sensitive to discern and identify potentially interesting biological differences between these different pathological conditions affecting the brain.

7. Age-dependent disruption of IRE-driven iron homeostasis in the 5XFAD mouse model

Alzheimer's disease is thought to develop over decades [39–41]. However, detailed molecular studies of AD brains can only be based on post-mortem tissues. To reveal the early molecular changes that initiate the progression to AD we must study the brains of animal disease models. Given that the IRE gene sets appear to work well in human datasets, we then tested our mouse IRE gene sets on an RNA-seq dataset derived from brain cortex tissue of the 5XFAD transgenic mouse AD model (GEO: GSE140286). The 5XFAD mouse is one of the most common systems used to model the amyloid beta and tau histopathologies of AD brains. It possesses two transgenes that include a total of five different mutations, each of which individually causes fAD in humans. In this dataset, the mice analysed were either 3, 6 or 12 months of age.

Using gene set enrichment testing methods as before, we observed significant enrichment of the *all 3' IREs* and *all 5' IREs* gene sets in several comparisons. These included 5XFAD vs. wild type comparisons and wild type aging comparisons (Bonferroni-adjusted enrichment p -value < 0.05) (**Figure 7A**). Notably, even the youngest age group of 5XFAD mutant mice (3 months) displayed significant enrichment of genes containing 3' or 5' IREs compared to age-matched wild types. This is consistent with an enrichment of immune-related Hallmark gene sets that we observed in this age group (see **Figure 7B**) and with a previous transcriptome analysis suggesting immune activation in 5XFAD mice as early as 2–4 months [42]. UpSet plots of overlapping leading-edge genes suggest that the IRE responses due to aging and due to the 5XFAD transgenes may involve partially overlapping gene expression changes (**Figure 8**). In addition, the UpSet plots reveal subsets containing large numbers of IRE-containing genes which uniquely contribute to enrichment of IRE gene sets in only one comparison (e.g. 256 3' IRE genes only contribute to enrichment in the "5xFAD vs WT at 6 months" comparison). Notably, there are 126 shared 3' IRE genes contributing to enrichment in the 5xFAD vs WT at 6 months" and 5xFAD vs WT at 3 months" comparisons,

but no genes shared between these comparisons and the 5xFAD vs WT at 12 months" comparison. This suggests that enrichment of predicted IRE-genes (and hence the IRP/IRE-mediated response) may vary greatly between ages for this mouse AD model. Although beyond the scope of our current analysis, these subsets of genes may represent biologically distinct age-dependent iron dyshomeostasis responses caused by the transgenes which may be worthy of future investigation.

8. Similarities in IRE-driven iron homeostasis responses during hypoxia and a familial AD-like mutation in a zebrafish model

Concerns have been raised over the relevance of transgenic mouse models in modelling the early stages of AD (reviewed by [43]). In contrast, knock-in models of fAD only exhibit subtle pathological changes with little to no visible amyloid or tau pathology present [44]. However, because they more closely mimic the genetic state of fAD, knock-in models may reveal the early molecular changes that drive later fAD pathology. We had access to whole-brain RNA-seq data from a knock-in zebrafish model of fAD possessing a single fAD-like mutation in its endogenous *psen1* gene (*psen1*^{Q96_K97del/+}). Previous analysis of a subset of this dataset involving young adults (6-month-old brains) revealed gene expression changes related to altered energy metabolism [45]. (In contrast, the 3-month-old young adult 5XFAD mouse brain dataset is dominated by immune/inflammation responses, **Figure 7B**). Considering the critical role of iron homeostasis in energy metabolism, we decided to revisit this zebrafish dataset. We performed IRE gene set enrichment on the entire dataset in order to include exploration of the effects of aging and acute hypoxia (two important risk factors for sporadic late onset AD) and to analyse how these effects interact with the fAD-like *psen1*^{Q96_K97del/+} mutant genotype. The experimental design and the results of the differential gene expression analyses and gene set enrichment tests are summarised in **Figure 9**.

We first turned our attention to the comparison between young adult (6-month-old) *psen1*^{Q96_K97del/+} mutant zebrafish and their wild-type siblings. At this age, gene expression changes in the mutant fish likely represent early stresses driving the development of fAD in humans. Gene set enrichment tests in this comparison identify alteration of energy metabolism-related Hallmark gene sets (e.g. OXIDATIVE PHOSPHORYLATION, GLYCOLYSIS) (**Figure 9B**) which is consistent with a previous analysis of gene ontology terms with this dataset [45]. In addition, we see enrichment of other gene sets including FATTY ACID METABOLISM, PI3K AKT MTOR SIGNALLING, MTORC1 SIGNALLING, and HEME METABOLISM. All of these gene sets which show enrichment in 6-month-old *psen1*^{Q96_K97del/+} mutants relative to wild-type siblings are also enriched in 24-month-old *psen1*^{Q96_K97del/+} mutants relative to their wild-type siblings (**Figure 9B**). This supports that the biological activities represented in these gene sets are amongst the earliest altered in this particular fAD mutation model.

In Lumsden et al. [16] we predicted that fAD mutations in the major locus *PSEN1* would cause an early cellular deficiency of ferrous iron due to the observation of insufficient acidification of the endolysosomal pathway in in-vitro *PSEN1* mutation studies [46,47]. In Newman et al. [45] we saw that GO analysis of 6 month old *psen1*^{Q96_K97del/+} zebrafish brain supported that lysosomal acidification was affected. Therefore, we decided to apply our IRE

enrichment analysis to test for evidence of iron dyshomeostasis in these fish. The enrichment of the *all 3' IREs* set in 6 month old *psen1^{Q96_K97del/+}* zebrafish brains supports that iron dyshomeostasis is an important stress in the early stages of fAD (**Figure 10A**).

While almost all pairwise comparisons in the zebrafish dataset show significant enrichment of at least one IRE gene set (**Figure 10A**), the expression of IRE genes appears to differ in terms of the proportions of IRE-containing transcripts which show increased versus decreased abundance (**Figure 10B**). In addition, the Principal Component Analysis plot of expression of the *all 3' IREs* set over all samples shown in **Figure 10C** suggests that different conditions appear to have distinct expression patterns of these genes. Across the first principal component, different age groups (6- and 24-month-old brains) differ in their expression of predicted 3' IRE genes, while the second principal component appears to separate *psen1^{Q96_K97del/+}* mutants from their wild-type siblings. This separation between *psen1^{Q96_K97del/+}* mutants and wild type siblings is even more pronounced when both are exposed to hypoxia.

To gain more insight into the similarities and differences between the IRE responses in the *psen1^{Q96_K97del/+}* vs. wild type comparison, we plotted UpSet plots of overlapping leading-edge genes (**Figure 10D**). These plots suggest that the IRE responses during hypoxia, aging, and due to this fAD-like mutation are mostly distinct from each other with unique leading-edge genes. However, similarities in the IRE response between different conditions are suggested by the existence of some shared leading-edge genes. For example, for the set of *all 3' IREs*, the “6-month-old *psen1^{Q96_K97del/+}* vs. wild type” comparison shares 19 leading-edge genes with the “24-month-old *psen1^{Q96_K97del/+}* vs. wild type” comparison. As an initial exploration of the biological relevance of these genes, we submitted them to the STRINGR tool. This indicated that the proteins products of these genes were significantly associated with each other (e.g. in terms of text-mining from Pubmed articles, experimentally determined interactions, and co-expression). These proteins were significantly over-represented in the sets “MAPK pathway”, “AP-1 transcription factor”, “Jun-like transcription factor”, and “signaling by TGF-beta family members” (FDR-adjusted over-representation p-value < 0.05; **Supplementary Figure 4**). The AP-1 and MAPK pathways have previously been shown to be stimulated by iron depletion [48,49]. Therefore, mechanistically, it is possible that the IRE-IRP response to iron dyshomeostasis in the fAD-like zebrafish mutant might involve these pathways, although this requires confirmation *in vivo*.

The fact that aging, hypoxia, and a fAD-like mutation all cause changes in the abundance of IRE-containing transcripts in zebrafish raised concerns regarding the specificity of such changes. Therefore, as a negative control, we examined changes in IRE transcript abundance in a brain transcriptome dataset derived from zebrafish heterozygous for a *psen1* mutation now thought not to be fAD-like, *psen1^{K97fs}* [50]. In this dataset, *psen1^{K97fs/+}* zebrafish are compared to their wild type siblings at 6 and 24 months. We tested this dataset for enrichment using our zebrafish 3' and 5' IRE gene sets but found no significant enrichment of any of our predicted IRE gene sets in *psen1^{K97fs/+}* vs. wild type comparisons at any age (**Table 4; Supplementary Figure 5**). Reassuringly, we still observed significant enrichment of both 3' and 5' IRE gene sets during wild type aging (24-month-old wild types vs. 6-month-old wild types), consistent with the equivalent comparison in the *psen1^{Q96_K97del/+}* dataset. These results support that IRE-containing transcript abundance changes are sufficiently sensitive to reflect differences in iron homeostasis between different mutation models.

9. Simultaneous stabilisation of some 3' IRE transcripts and destabilisation of others

In the cultured cell line dataset analysed above, we noticed that even a straightforward iron deficiency treatment resulted in the simultaneous increase and decrease in expression of 3' IRE-containing genes. These findings are difficult to reconcile with the current paradigm that stabilisation of 3' IRE-containing genes occurs under iron deficiency and suggest that the current model of the IRP/IRE system may be incomplete or insufficient for describing the regulation of non-canonical IREs. Given that many predicted 3' IRE genes with non-canonical IREs (e.g. in the *all 3' IREs* set) displayed enrichment and different gene expression patterns in the fAD-like zebrafish dataset, we decided to explore further the stability changes of these genes by comparing the expression of spliced and unspliced transcripts for each gene (**Supplementary Text 1**). We found that transcripts of some predicted 3' IRE genes were significantly increased in stability while others were significantly decreased in stability (**Supplementary Figure 5; Supplementary Table 4**).

Discussion

In this study we successfully identified sets of genes predicted to contain IREs in human, mouse, and zebrafish, and applied these gene sets to gain insight into the IRP/IRE system of post-transcriptional responses to iron dyshomeostasis. We found that IRE genes are generally not well-represented in the existing gene sets in MSigDB. Importantly, these gene sets are most significantly over-represented in an existing gene set previously shown to be up-regulated in AD brains (the “Blalock Alzheimer’s Disease Up” gene set from MSigDB). This supports the importance of iron dyshomeostasis in sporadic late onset Alzheimer’s disease. Furthermore, our IRE gene sets displayed significant enrichment in postmortem brains from a human AD cohort, from the 5XFAD mouse model, and from a zebrafish model of a fAD-like mutation. This demonstrates for the first time the involvement of a coordinated IRE-containing gene expression response to iron dyshomeostasis in the context of AD.

The relatively tightly controlled conditions in the mouse and zebrafish model datasets revealed a strong age-dependent effect on the transcript abundances of these predicted IRE-containing genes. Notably, 3' IRE gene expression changes were amongst the earliest changes observable in the zebrafish fAD-like mutation model alongside changes in energy metabolism. These 3' IRE gene expression changes preceded other signals of pathological change in the transcriptome (such as altered expression of inflammatory response pathways) commonly associated with AD. In addition, IRE gene sets were sufficiently sensitive to distinguish not only between iron overload and deficiency in a cultured cell line dataset, but also between AD and other pathological conditions affecting the brain (i.e. pathological aging and progressive supranuclear palsy). This suggests that the dysregulation of IRE-containing genes and iron homeostasis in AD may differ from other conditions. Whether iron deficiency or iron overload was present in the AD brain tissue samples (taken from either temporal cortex or cerebellum) was unclear.

Most previous work has assumed that accumulation of iron in the brain with age (a phenomenon observed broadly

across animal phyla [51,52]) is indicative of cellular iron overload. However, a recent publication by [53] showed that disturbed lysosomal function leading to increased lysosomal pH causes a deficiency of functional ferrous iron (Fe^{2+}) while non-functional ferric iron (Fe^{3+}) accumulated in lysosomes. The deleterious effects of this on the brains of mice (defective mitochondrial biogenesis and function and stimulation of inflammatory responses) could be alleviated by increasing the levels of iron in their diet. The observations of Nixon and colleagues that acidification of the endolysosomal pathway is affected both by fAD mutations in *PSEN1* [46] and excessive dosage of the *APP* gene [54], together with our observations from our fAD-like *psen1*^{Q96_K97del/+} mutant zebrafish, support the possibility that fAD brains may suffer a ferrous iron deficiency in a background of ferric iron overload. Intriguingly, the greatest genetic risk factor for late onset AD, the $\epsilon 4$ allele of the gene *APOE*, appears to increase lysosomal pH [55] but $\epsilon 4$'s increased risk of AD is alleviated in individuals who possess the *HFE* 282Y allele that predisposes to the iron overload disease hemochromatosis [56]. Given that many other risk loci for sporadic late onset AD also affect endolysosomal pathway function (reviewed in [57]) it is reasonable to suggest that disturbed iron homeostasis may afflict brains with this disease.

Outside our interest in AD, our analyses also revealed the surprising finding that 3' IRE-containing genes could be both upregulated and downregulated by iron deficiency (at least in a cultured cell line). We also observed simultaneous stabilisation of some 3'IRE transcripts and destabilisation of others in our analysis of zebrafish brains. This challenges the simplistic paradigm of stabilisation of 3' IRE-containing transcripts under ferrous iron deficiency. Previous research holds that under iron deficiency, 3' IRE-containing genes such as *DMT1* (*divalent metal transporter 1*) and *TFRC* (*transferrin receptor protein*) are stabilised and hence increased in expression [23] in order to increase ferrous iron availability. However, our findings reveal that this same principle may not apply to other, less-characterised 3' IRE-containing genes, including IREs deviating from the canonical IRE sequence. Many of these IRE-like sequences are likely to have some functionality [26–28], and their expression and stability changes in our analyses indicate that they are likely to be important in iron dyshomeostasis responses in AD. We emphasise the need to characterise further the stability of these predicted 3' IRE-containing transcripts under conditions of altered iron availability to better understand iron dyshomeostasis responses at the gene expression level.

Collectively, our results strengthen the known association of iron dyshomeostasis with both fAD and AD in general, while also demonstrating how changes in the stability and abundance of IRE-containing transcripts can be used to give insight into iron dyshomeostasis responses in different species, tissues, and conditions.

The limitations of our study, the conservation of IRE gene sets between species, and the role of iron dyshomeostasis in AD are discussed further in **Supplementary Text 2**.

Materials and Methods

Reproducibility.

Please see github.com/UofABioinformaticsHub/ireAnalysis for code to reproduce all analyses described below, in addition to .gtf files and R objects including the IRE gene sets for human, mouse, and zebrafish.

Defining IRE gene sets for human, mouse, and zebrafish.

We extracted all 3' and 5' UTR sequences from the human, mouse and zebrafish genome assemblies using the Bioconductor packages *BSgenome.Hsapiens.UCSC.hg38*, *BSgenome.Mmusculus.UCSC.mm10* and *BSgenome.Drerio.UCSC.danRer11*, and gene definitions from the Ensembl 94 release. Each set of UTR sequences was then submitted input into the SIREs web server (v.2.0 [24]). The SIREs algorithm assigns quality scores to predicted IREs taking into account whether the sequence is canonical, whether it contains any mismatches and bulges, and the free energy of the secondary structure. Canonical sequences are tagged by SIREs as being high-quality, while IRE-like sequences are tagged as low or medium quality. Given that High-quality IRE predictions miss the majority of true IREs, this enables a more comprehensive sampling of IRE motifs. For human, mouse, and zebrafish, we separately defined the following four gene sets: **HQ 3' IREs** and **HQ 5' IREs** (representing genes with high-quality predicted IREs), along with **all 3' IREs** and **all 5' IREs**, which included genes containing any predicted IRE in the respective UTR. Comparisons between gene sets were performed using the UpSetR package (v.1.4.0 [58]) with mappings between species obtained by BioMart [59].

Over-representation of IRE gene sets in existing MSigDB gene sets.

We downloaded the following gene set collections from MSigDB (v.6.0 [60]): Hallmark, C2 (gene sets from online pathway databases and biomedical literature, including KEGG and the REACTOME databases), C3 (motif gene sets based on regulatory targets), and C5 (gene sets defined by Gene Ontology terms). We excluded the following collections from analysis: C1 (specific to human chromosomes and cytogenetic bands, while our analysis involves different species), C4 (computationally-defined cancer-focused gene sets), C6 (oncogenic signatures) and C7 (immunologic signatures). C4, C6, and C7 were not included as the level of detail in the gene sets in these specific collections is more domain-specific rather than broad-level. We used Fisher's exact test to determine whether any IRE geneset was significantly over-represented in each MSigDB gene set. Gene sets were defined as having significant enrichment for IRE gene sets if the FDR-adjusted *p*-value from Fisher's exact test was below 0.05. UpSet plots were produced using the UpSetR package (v.1.4.0 [58]) while network representations were produced in Gephi (v.0.9.3 [61]). To produce network visualisations, we exported node and edge tables from R. The nodes table contained the following gene sets: top 15 gene sets (ranked by Fisher's exact test *p*-value), Hallmark Heme Metabolism gene set, **all 3' IREs**, **all 5' IREs**, and all genes contained within these gene sets. The edges table contained gene – gene set edges which indicated the gene set(s) that genes belonged to. To create the network plots, we used "Force Atlas 2" as the initial layout algorithm, followed by the "Yifan Hu" [62] layout algorithm to improve the separation between groups of genes.

Over-representation analysis of transcription factor motifs in IRE gene promoters. Defining promoter regions as being 1500 bp upstream and 200 bp downstream of the transcription start site for each gene, we used the findMotifs.pl script from HOMER (v.4.11) [63,64] to search for known transcription factor binding site (TFBS) motifs in the promoters of each IRE gene set. The HOMER Motif database contains 363 vertebrate transcription factor binding motifs based on analysis of high-quality public ChIP-seq datasets (<http://homer.ucsd.edu/homer/motif/HomerMotifDB/homerResults.html>). We considered TFBS motifs as being significantly enriched in a gene set if the FDR-adjusted *p*-value was less than 0.05.

Gene set enrichment testing. We performed all gene set enrichment tests in R v3.6.1 [65] using *fry* [32,33], *camera* [34], and *fgsea* [35,36]. For *fry*, and *camera*, we used model fits obtained using *limma* [66,67], whilst for *fgsea*, a ranked list was obtained using *moderated t*-statistics taken from *limma*. All genes were used in gene set enrichment tests (i.e. not just DE genes). We combined the raw *p*-values from *fry*, *camera*, and *fgsea* using Wilkinson's method [68] with default parameters, followed by FDR-adjustment. All of this functionality is included in the *combinedGSEA* function (see GitHub). When performing gene set enrichment testing on the MSigDB Hallmark gene sets, we applied FDR-adjustment to combined *p*-values and defined significant enrichment as gene sets having an adjusted *p*-value < 0.05. When performing gene set enrichment on the four IRE gene sets (*all 3' IREs*, *all 5' IREs*, *HQ 3' IREs*, *HQ 5' IREs*), we applied Bonferroni-adjustment to combined *p*-values to further protect against Type I errors and defined significant enrichment as gene sets having an adjusted *p*-value < 0.05. Depending on the species in the dataset being analysed, we used the respective IRE gene sets defined for human, mouse, or zebrafish.

Analysis of the Caco-2 cultured cell line dataset. We downloaded processed microarray data from the GEO dataset GSE3573. This study investigated gene expression responses to iron treatments, including iron deficiency (cells treated with ferric ammonium citrate), and iron overload (cells grown in DMEM-FBS medium with hemin) [69]. We performed differential gene expression analysis using the “lmFit” and eBayes” functions in *limma* [66]. Genes were defined as differentially expressed when their FDR-adjusted *p*-value < 0.05.

Analysis of the Mayo Clinic RNA-seq dataset. We downloaded processed CPM count data from Synapse (<https://www.synapse.org/#!/Synapse:syn5550404>). We matched cerebellum and temporal cortex samples by their patient ID, and only retained genes which were present across all samples and patients for which there were both cerebellum and temporal cortex samples (n=236 patients with measurements for cerebellum and temporal cortex, 472 samples in total). We performed analysis using *limma* [66,67] and determined differentially expressed genes between conditions. In addition, we used the “duplicateCorrelation” function in *limma*, setting the “block” parameter to the patient ID. Genes were considered differentially expressed if their FDR-adjusted *p*-value < 0.05.

fAD-like *psen1*^{Q96_K97del/+} zebrafish. The isolation of the *psen1*^{Q96_K97del} mutation has previously been described [45].

Mutations were only analysed in the heterozygous state in this study.

Hypoxia treatment of female adult zebrafish. *psen1*^{Q96-K97del/+} mutants and their wild-type siblings were treated in low oxygen levels by placing zebrafish in oxygen-depleted water for 3 hours (oxygen concentration of 6.6 ± 0.2 mg/L in normoxia and 0.6 ± 0.2 mg/L in hypoxia).

Whole brain removal from adult zebrafish. After normoxia or hypoxia treatment adult fish were euthanized by sudden immersion in an ice water slurry for at least ~30 seconds before decapitation and removal of the entire brain for immediate RNA or protein extraction. All fish brains were removed during late morning/noon to minimise any influence of circadian rhythms.

RNA extraction from whole brain.

Total RNA was isolated from heterozygous mutant and WT siblings using the *mirVana* miRNA isolation kit (Thermo Fisher). RNA isolation was performed according to the manufacturer's protocol. First a brain was lysed in a denaturing lysis solution. The lysate was then extracted once with acid-phenol:chloroform leaving a semi-pure RNA sample. The sample was then purified further over a glass-fiber filter to yield total RNA. Total RNA was DNase treated using the DNA-free™ Kit from Ambion, Life Technologies according to the manufacturer's instructions. Total RNA was then sent to the Genomics Facility at the South Australian Health and Medical Research Institute (Adelaide, Australia) to assess RNA quality and for subsequent RNA sequencing (using *poly-A enriched RNA-seq technology*, and *estimated gene expression from the resulting single-end 75 bp reads using the reference GRCz11 zebrafish assembly transcriptome*)

Pre-processing of RNA-seq data for fAD-like zebrafish dataset. RNA-seq libraries contained single-end 75bp Illumina NextSeq reads. We performed quality trimming with *AdapterRemoval* using default parameters, followed by quality assessment with FastQC and ngsReports. Trimmed reads were pseudo-aligned to the reference zebrafish transcriptome using *Kallisto* (v.0.45) [70] and transcript descriptions from Ensembl release 94. The “catchKallisto” function from *edgeR* [71] was used to import and summarise counts from transcript-level to gene-level, with all subsequent analyses performed at the gene-level.

Differential gene expression analysis for fAD-like zebrafish dataset. For differential gene expression analysis, we retained all genes with expression of at least 1 cpm in 4 or more samples, and used *voomWithQualityWeights* to downweight lower quality samples [67]. Contrasts were defined to include all relevant pairwise comparisons between conditions, and genes were considered as differentially expressed using an FDR-adjusted *p*-value < 0.05.

Estimation of spliced and unspliced gene expression in fAD-like zebrafish dataset. For spliced transcripts in Ensembl release 94, we additionally defined unspliced genes including intronic regions. Unspliced transcripts were appended to the end of the reference transcriptome and used to build a new *Kallisto* [70] index. Estimated counts for spliced transcripts and unspliced genes were imported into R using the “catchKallisto” function from *edgeR* [71].

Gene set enrichment tests for non-fAD-like (K97fs/+) zebrafish dataset. Please refer to [45] for details on RNA-seq data processing and analysis of the non-fAD-like dataset. In the current work, we used the gene expression counts matrix with *limma*. The voom, design, and contrasts objects produced as part of the *limma* analysis were used for gene set enrichment analysis with the zebrafish IRE gene sets we defined as well as the MSigDB Hallmark gene sets. Significantly enriched Hallmark gene sets had FDR-adjusted p -value < 0.05 while IRE gene sets were considered significantly enriched if the Bonferroni-adjusted p -value < 0.05 .

Gene set enrichment tests for 7-day-old Q96_K97del/+ dataset. Please refer to Dong et al. (GEO accession: GSE148631, manuscript in preparation) for details on RNA-seq data processing and analysis. In the current work, we used the gene expression counts matrix with *limma* to perform gene set enrichment analysis. IRE gene sets we defined as well as the MSigDB Hallmark gene sets. Significantly enriched Hallmark gene sets had FDR-adjusted p -value < 0.05 while IRE gene sets were considered significantly enriched if the Bonferroni-adjusted p -value < 0.05 .

Differential transcript stability analysis. The estimated spliced and unspliced transcript count estimates from *kallisto* [70] were imported into R using the *catchKallisto* function from *edgeR* [71]. We used *limma* [66] to determine the logFC of spliced transcripts and unspliced transcripts for each comparison. To test for whether there was a significant difference in the logFC of the spliced and unspliced transcripts, we used Welch's t -test with the *s2.prior* values from *limma* as the variances of the spliced and unspliced transcripts. We defined the null (no stabilisation of transcript) and alternate (stabilisation of transcript) hypotheses for each gene as follows, where s and u refer to the spliced and unspliced versions of a particular gene:

$$H_0: \log FC_s = \log FC_u$$

$$H_a: \log FC_s \neq \log FC_u$$

We defined genes with FDR-adjusted p -values < 0.05 as having differential stability.

Neural cell type proportion. The Mayo Clinic RNA-seq study, 5XFAD mice, and fAD-like zebrafish datasets are bulk RNA-seq datasets. To confirm that any gene expression changes were likely due to altered transcriptional programs rather than changes in cell type proportions, we compared expression of marker genes for four common neural cell types (astrocytes, neurons, oligodendrocytes, microglia) in conditions within each dataset. The marker genes for astrocytes, neurons, and oligodendrocytes were obtained from MSigDB gene sets from [72] which were based on studies in mice. The marker genes for microglia were derived from [73] which was based on studies in human and mouse. All gene IDs were converted to human, mouse, or zebrafish Ensembl IDs using BioMart [59] for each dataset.

References

1. Ostrowitzki S, Lasser RA, Dorflinger E, Scheltens P, Barkhof F, Nikolcheva T, et al. A phase III randomized trial of gantenerumab in prodromal Alzheimer's disease. *Alzheimer's Res Ther.* BioMed Central Ltd.; 2017;9.
2. Doody RS, Raman R, Farlow M, Iwatsubo T, Vellas B, Joffe S, et al. A phase 3 trial of semagacestat for treatment of Alzheimer's disease. *N Engl J Med.* Massachusetts Medical Society; 2013;369:341–50.
3. Doody RS, Thomas RG, Farlow M, Iwatsubo T, Vellas B, Joffe S, et al. Phase 3 trials of solanezumab for mild-to-moderate Alzheimer's disease. *N Engl J Med* [Internet]. Massachusetts Medical Society; 2014 [cited 2020 Apr 30];370:311–21. Available from: <http://www.nejm.org/doi/pdf/10.1056/NEJMoa1312889>
4. Honig LS, Vellas B, Woodward M, Boada M, Bullock R, Borrie M, et al. Trial of solanezumab for mild dementia due to Alzheimer's disease. *N Engl J Med.* Massachusetts Medical Society; 2018;378:321–30.
5. Bartzokis G, Sultzer D, Mintz J, Holt LE, Marx P, Kelly Phelan C, et al. In vivo evaluation of brain iron in Alzheimer's disease and normal subjects using MRI. *Biol Psychiatry.* 1994;35:480–7.
6. Bartzokis G, Tishler TA. MRI evaluation of basal ganglia ferritin iron and neurotoxicity in Alzheimer's and Huntington's disease. *Cell Mol Biol (Noisy-le-grand).* 2000;46:821–33.
7. Ding B, Chen KM, Ling HW, Sun F, Li X, Wan T, et al. Correlation of iron in the hippocampus with MMSE in patients with Alzheimer's disease. *J Magn Reson Imaging.* 2009;29:793–8.
8. Langkammer C, Ropele S, Pirpamer L, Fazekas F, Schmidt R. MRI for iron mapping in Alzheimer's disease. *Neurodegener Dis.* 2014;13:189–91.
9. Van Duijn S, Bulk M, Van Duinen SG, Nabuurs RJA, Van Buchem MA, Van Der Weerd L, et al. Cortical Iron Reflects Severity of Alzheimer's Disease. *J Alzheimer's Dis.* IOS Press; 2017;60:1533–45.
10. Mantyh PW, Ghilardi JR, Rogers S, DeMaster E, Allen CJ, Stimson ER, et al. Aluminum, Iron, and Zinc Ions Promote Aggregation of Physiological Concentrations of β -Amyloid Peptide. *J Neurochem.* 1993;61:1171–4.
11. Liu B, Moloney A, Meehan S, Morris K, Thomas SE, Serpell LC, et al. Iron promotes the toxicity of amyloid β peptide by impeding its ordered aggregation. *J Biol Chem.* 2011;286:4248–56.
12. Lovell MA, Robertson JD, Teesdale WJ, Campbell JL, Markesbery WR. Copper, iron and zinc in Alzheimer's disease senile plaques. *J Neurol Sci.* 1998;158:47–52.
13. Meadowcroft MD, Peters DG, Dewal RP, Connor JR, Yang QX. The effect of iron in MRI and transverse relaxation of amyloid-beta plaques in Alzheimer's disease. *NMR Biomed.* John Wiley and Sons Ltd; 2015;28:297–305.
14. Telling ND, Everett J, Collingwood JF, Dobson J, van der Laan G, Gallagher JJ, et al. Iron Biochemistry is Correlated with Amyloid Plaque Morphology in an Established Mouse Model of Alzheimer's Disease. *Cell Chem Biol.* Elsevier Ltd; 2017;24:1205–1215.e3.
15. Selkoe DJ, Hardy J. The amyloid hypothesis of Alzheimer's disease at 25 years. *EMBO Mol Med.* EMBO; 2016;8:595–608.
16. Lumsden AL, Rogers JT, Majd S, Newman M, Sutherland GT, Verdile G, et al. Dysregulation of neuronal iron homeostasis as an alternative unifying effect of mutations causing familial Alzheimer's disease. *Front Neurosci.* Frontiers Media S.A.; 2018;12:533.
17. Masaldan S, Belaidi AA, Ayton S, Bush AI. Cellular senescence and iron dyshomeostasis in Alzheimer's disease. *Pharmaceuticals.* MDPI AG; 2019.
18. Lane DJR, Merlot AM, Huang MLH, Bae DH, Jansson PJ, Sahni S, et al. Cellular iron uptake, trafficking and metabolism: Key molecules and mechanisms and their roles in disease. *Biochim. Biophys. Acta - Mol. Cell Res.* Elsevier; 2015. p. 1130–44.
19. Gray NK, Hentze MW. Iron regulatory protein prevents binding of the 43S translation pre-initiation complex to ferritin and eALAS mRNAs. *EMBO J.* Wiley; 1994;13:3882–91.
20. Hentze MW, Muckenthaler MU, Andrews NC. Balancing acts: Molecular control of mammalian iron metabolism. *Cell.* Cell Press; 2004. p. 285–97.
21. Muckenthaler MU, Galy B, Hentze MW. Systemic Iron Homeostasis and the Iron-Responsive Element/Iron-Regulatory Protein (IRE/IRP) Regulatory Network. *Annu Rev Nutr* [Internet]. Annual Reviews; 2008 [cited 2020 Apr 30];28:197–213. Available from: <http://www.annualreviews.org/doi/10.1146/annurev.nutr.28.061807.155521>
22. Basilion JP, Rouault TA, Massinople CM, Klausner RD, Burgesst WH. The iron-responsive element-binding protein: Localization of the RNA-binding site to the aconitase active-site cleft (UV cross-linking/base hydrolysis). *Biochemistry.* 1994.
23. Pantopoulos K. Iron metabolism and the IRE/IRP regulatory system: An update. *Ann. N. Y. Acad. Sci. New York Academy of Sciences;* 2004. p. 1–13.
24. Campillos M, Cases I, Hentze MW, Sanchez M. SIREs: searching for iron-responsive elements. *Nucleic Acids Res* [Internet]. 2010 [cited 2020 Apr 30];38:W360–367. Available from: <http://ccbg.imppc.org/sires/index.html>
25. Goforth JB, Anderson SA, Nizzi CP, Eisenstein RS. Multiple determinants within iron-responsive elements dictate iron regulatory protein binding and regulatory hierarchy. *RNA.* 2010;16:154–69.
26. Henderson BR, Menotti E, Kühn LC. Iron regulatory proteins 1 and 2 bind distinct sets of RNA target sequences. *J Biol Chem.* 1996;271:4900–8.
27. Henderson BR, Menotti E, Bonnard C, Kühn LC. Optimal sequence and structure of iron-responsive elements. Selection of RNA stem-loops with high affinity for iron regulatory factor. *J Biol Chem.* 1994;269:17481–9.

28. Butt J, Kim HY, Basilion JP, Cohen S, Iwai K, Philpott CC, et al. Differences in the RNA binding sites of iron regulatory proteins and potential target diversity. *Proc Natl Acad Sci U S A. National Academy of Sciences*; 1996;93:4345–9.
29. Surinya KH, Cox TC, May BK. Identification and characterization of a conserved erythroid-specific enhancer located in intron 8 of the human 5-aminolevulinic synthase 2 gene. *J Biol Chem. American Society for Biochemistry and Molecular Biology Inc.*; 1998;273:16798–809.
30. Theil EC. Regulation of ferritin and transferrin receptor mRNAs. *J. Biol. Chem.* 1990. p. 4771–4.
31. Alhamdoosh M, Law CW, Tian L, Sheridan JM, Ng M, Ritchie ME. Easy and efficient ensemble gene set testing with EGSEA. *F1000Research. Faculty of 1000 Ltd*; 2017;6:2010.
32. Wu D, Lim E, Vaillant F, Asselin-Labat M-L, Visvader JE, Smyth GK. ROAST: rotation gene set tests for complex microarray experiments. *Bioinformatics [Internet]*. 2010 [cited 2020 Apr 30];26:2176–82. Available from: www.bioconductor.org
33. Giner G, Smyth GK, Giner G, Smyth GK. <p>FRY: a fast approximation to ROAST gene set test with mean aggregated set statistics</p>. *F1000Research*. 2016;5.
34. Wu D, Smyth GK. Camera: a competitive gene set test accounting for inter-gene correlation. *Nucleic Acids Res [Internet]*. 2012 [cited 2020 Apr 30];40:e133. Available from: <https://academic.oup.com/nar/article-abstract/40/17/e133/2411151>
35. Sergushichev AA. An algorithm for fast preranked gene set enrichment analysis using cumulative statistic calculation. *bioRxiv [Internet]*. Cold Spring Harbor Laboratory; 2016 [cited 2020 Apr 30];060012. Available from: <http://dx.doi.org/10.1101/060012> <https://www.biorxiv.org/content/10.1101/060012v1>
36. Subramanian A, Tamayo P, Mootha VK, Mukherjee S, Ebert BL, Gillette MA, et al. Gene set enrichment analysis: A knowledge-based approach for interpreting genome-wide expression profiles. *Proc Natl Acad Sci U S A. National Academy of Sciences*; 2005;102:15545–50.
37. Allen M, Carrasquillo MM, Funk C, Heavner BD, Zou F, Younkin CS, et al. Human whole genome genotype and transcriptome data for Alzheimer's and other neurodegenerative diseases. *Sci Data. Nature Publishing Groups*; 2016;3:1–10.
38. Ossenkoppele R, Van Berckel BN, Prins ND. Amyloid imaging in prodromal Alzheimer's disease. *Alzheimer's Res. Ther. BioMed Central*; 2011. p. 26.
39. Protas HD, Chen K, Langbaum JBS, Fleisher AS, Alexander GE, Lee W, et al. Posterior cingulate glucose metabolism, hippocampal glucose metabolism, and hippocampal volume in cognitively normal, late-middle-aged persons at 3 levels of genetic risk for alzheimer disease. *JAMA Neurol. American Medical Association*; 2013;70:320–5.
40. Caldwell CC, Yao J, Brinton RD. Targeting the Prodromal Stage of Alzheimer's Disease: Bioenergetic and Mitochondrial Opportunities. *Neurotherapeutics [Internet]*. Springer New York LLC; 2015 [cited 2020 Apr 30];12:66–80. Available from: <http://link.springer.com/10.1007/s13311-014-0324-8>
41. Vermunt L, Sikkes SAM, van den Hout A, Handels R, Bos I, van der Flier WM, et al. Duration of preclinical, prodromal, and dementia stages of Alzheimer's disease in relation to age, sex, and APOE genotype. *Alzheimer's Dement. Elsevier Inc.*; 2019;15:888–98.
42. Bundy JL, Vied C, Badger C, Nowakowski RS. Sex-biased hippocampal pathology in the 5XFAD mouse model of Alzheimer's disease: A multi-omic analysis. *J Comp Neurol. Wiley-Liss Inc.*; 2019;527:462–75.
43. Drummond E, Wisniewski T. Alzheimer's disease: experimental models and reality. *Acta Neuropathol. Springer Verlag*; 2017. p. 155–75.
44. Xia D, Watanabe H, Wu B, Lee SH, Li Y, Tsvetkov E, et al. Presenilin-1 knockin mice reveal loss-of-function mechanism for familial alzheimer's disease. *Neuron. Cell Press*; 2015;85:967–81.
45. Newman M, Hin N, Pederson S, Lardelli M. Brain transcriptome analysis of a familial Alzheimer's disease-like mutation in the zebrafish presenilin 1 gene implies effects on energy production. *Mol Brain [Internet]*. BioMed Central Ltd.; 2019 [cited 2020 Apr 30];12:43. Available from: <https://molecularbrain.biomedcentral.com/articles/10.1186/s13041-019-0467-y>
46. Lee JH, Yu WH, Kumar A, Lee S, Mohan PS, Peterhoff CM, et al. Lysosomal proteolysis and autophagy require presenilin 1 and are disrupted by Alzheimer-related PS1 mutations. *Cell. Elsevier*; 2010;141:1146–58.
47. Lee JH, McBrayer MK, Wolfe DM, Haslett LJ, Kumar A, Sato Y, et al. Presenilin 1 Maintains Lysosomal Ca²⁺ Homeostasis via TRPML1 by Regulating vATPase-Mediated Lysosome Acidification. *Cell Rep. Elsevier B.V.*; 2015;12:1430–44.
48. Yu Y, Richardson DR. Cellular iron depletion stimulates the JNK and p38 MAPK signaling transduction pathways, dissociation of ASK1-thioredoxin, and activation of ASK1. *J Biol Chem.* 2011;286:15413–27.
49. Riera H, Afonso V, Collin P, Lomri A. A Central Role for JNK/AP-1 Pathway in the Pro-Oxidant Effect of Pyrrolidine Dithiocarbamate through Superoxide Dismutase 1 Gene Repression and Reactive Oxygen Species Generation in Hematopoietic Human Cancer Cell Line U937. *Papa S, editor. PLoS One [Internet]*. Public Library of Science; 2015 [cited 2020 Apr 30];10:e0127571. Available from: <https://dx.plos.org/10.1371/journal.pone.0127571>
50. Hin N, Newman M, Kaslin J, Douek AM, Lumsden A, Nik SHM, et al. Accelerated brain aging towards transcriptional inversion in a zebrafish model of the K115fs mutation of human PSEN2. *PLoS One. Public Library of Science*; 2020;15:e0227258.
51. Zecca L, Youdim MBH, Riederer P, Connor JR, Crichton RR, Stankowski JN, et al. Iron-export ferroxidase activity of β -amyloid precursor protein is inhibited by zinc in Alzheimer's disease. *Cell [Internet]*. BioMed Central Ltd; 2011 [cited 2020 Apr 30];142:359. Available from: <http://www.ncbi.nlm.nih.gov/pubmed/17987043>
52. Jacomin A-C, Geraki K, Brooks J, Tjendana-Tjhin V, Collingwood JF, Nezis IP. Impact of Autophagy and Aging on Iron Load and Ferritin in Drosophila Brain. *Front Cell Dev Biol [Internet]*. Frontiers Media S.A.; 2019 [cited 2020 Apr 30];7:142. Available from: <https://www.frontiersin.org/article/10.3389/fcell.2019.00142/full>
53. Yambire KF, Rostosky C, Watanabe T, Pacheu-Grau D, Torres-Odio S, Sanchez-Guerrero A, et al. Impaired lysosomal acidification triggers iron deficiency and inflammation in vivo. *Elife. eLife Sciences Publications Ltd*; 2019;8.
54. Jiang Y, Sato Y, Im E, Berg M, Bordini M, Darji S, et al. Lysosomal dysfunction in down syndrome is app-dependent and mediated by APP- β CTF (c99). *J Neurosci. Society for Neuroscience*; 2019;39:5255–68.
55. Prasad H, Rao R. Amyloid clearance defect in ApoE4 astrocytes is reversed by epigenetic correction of endosomal pH. *Proc Natl Acad Sci U S A. National Academy of Sciences*; 2018;115:E6640–9.
56. Tisato V, Zuliani G, Vigliano M, Longo G, Franchini E, Secchiero P, et al. Gene-gene interactions among coding genes of iron-homeostasis proteins and APOE-alleles in cognitive impairment diseases. *Ginsberg SD, editor. PLoS One [Internet]*. Public Library of Science; 2018 [cited 2020 Apr 30];13:e0193867. Available from: <https://dx.plos.org/10.1371/journal.pone.0193867>
57. Van Acker ZP, Bretou M, Annaert W. Endo-lysosomal dysregulations and late-onset Alzheimer's disease: Impact of genetic risk factors. *Mol. Neurodegener. BioMed Central Ltd.*; 2019. p. 1–20.
58. Conway JR, Lex A, Gehlenborg N. UpSetR: an R package for the visualization of intersecting sets and their properties. [cited 2020 Apr 30]; Available from: <https://gehlenborglab.shinyapps.io/>
59. Smedley D, Haider S, Ballester B, Holland R, London D, Thorisson G, et al. BioMart - Biological queries made easy. *BMC Genomics [Internet]*. BioMed Central; 2009 [cited 2020 Apr 30];10:22. Available from: <http://bmcbgenomics.biomedcentral.com/articles/10.1186/1471-2164-10-22>
60. Liberzon A, Subramanian A, Pinchback R, Thorvaldsdóttir H, Tamayo P, Mesirov JP, et al. Databases and ontologies Molecular signatures database (MSigDB) 3.0. *Bioinformatics [Internet]*. 2011 [cited 2020 Apr 30];27:1739–40. Available from: <http://www.broadinstitute.org/msigdb>
61. Bastian M, Heymann S, Jacomy M. Gephi: An Open Source Software for Exploring and Manipulating Networks Visualization and Exploration of Large Graphs [Internet]. *Third Int. AAAI Conf. Weblogs Soc. Media. 2009 Mar*. Available from: www.aaai.org
62. Hu Y. Algorithms for Visualizing Large Networks. 2011.
63. Benner C. HOMER (Hypergeometric Optimization of Motif EnRichment) [Internet]. Available from: <http://homer.ucsd.edu/homer/>
64. Heinz S, Benner C, Spann N, Bertolino E, Lin YC, Laslo P, et al. Simple Combinations of Lineage-Determining Transcription Factors Prime cis-Regulatory Elements Required for Macrophage and B Cell Identities. *Mol Cell.* 2010;38:576–99.
65. Team RC. R: A language and environment for statistical computing [Internet]. Vienna, Austria: R Foundation for Statistical Computing; 2018. Available from: <https://www.r-project.org/>
66. Ritchie ME, Phipson B, Wu D, Hu Y, Law CW, Shi W, et al. Limma powers differential expression analyses for RNA-sequencing and microarray studies. *Nucleic Acids Res. Oxford University Press*; 2015;43:e47.
67. Law CW, Chen Y, Shi W, Smyth GK. Voom: Precision weights unlock linear model analysis tools for RNA-seq read counts. *Genome Biol.* 2014;15.
68. Wilkinson B. A statistical consideration in psychological research. *Psychol Bull.* 1951;48:156–8.
69. Chicault C, Toutain B, Monnier A, Aubry M, Fergelot P, Le Treut A, et al. Iron-related transcriptomic variations in CaCo-2 cells, an in vitro model of intestinal absorptive cells. *Physiol Genomics.* 2006;26:55–67.
70. Bray NL, Pimentel H, Melsted P, Pachter L. Near-optimal probabilistic RNA-seq quantification. *Nat Biotechnol. Nature Publishing Group*; 2016;34:525–7.
71. Robinson MD, McCarthy DJ, Smyth GK. edgeR: A Bioconductor package for differential expression analysis of digital gene expression data. *Bioinformatics. Oxford University Press*; 2009;26:139–40.
72. Lein ES, Hawrylycz MJ, Ao N, Ayres M, Bensinger A, Bernard A, et al. Genome-wide atlas of gene expression in the adult mouse brain. *Nature.* 2007;445:168–76.
73. Bonham LW, Sirkis DW, Yokoyama JS. The transcriptional landscape of microglial genes in aging and neurodegenerative disease. *Front Immunol. Frontiers Media S.A.*; 2019;10:1170.

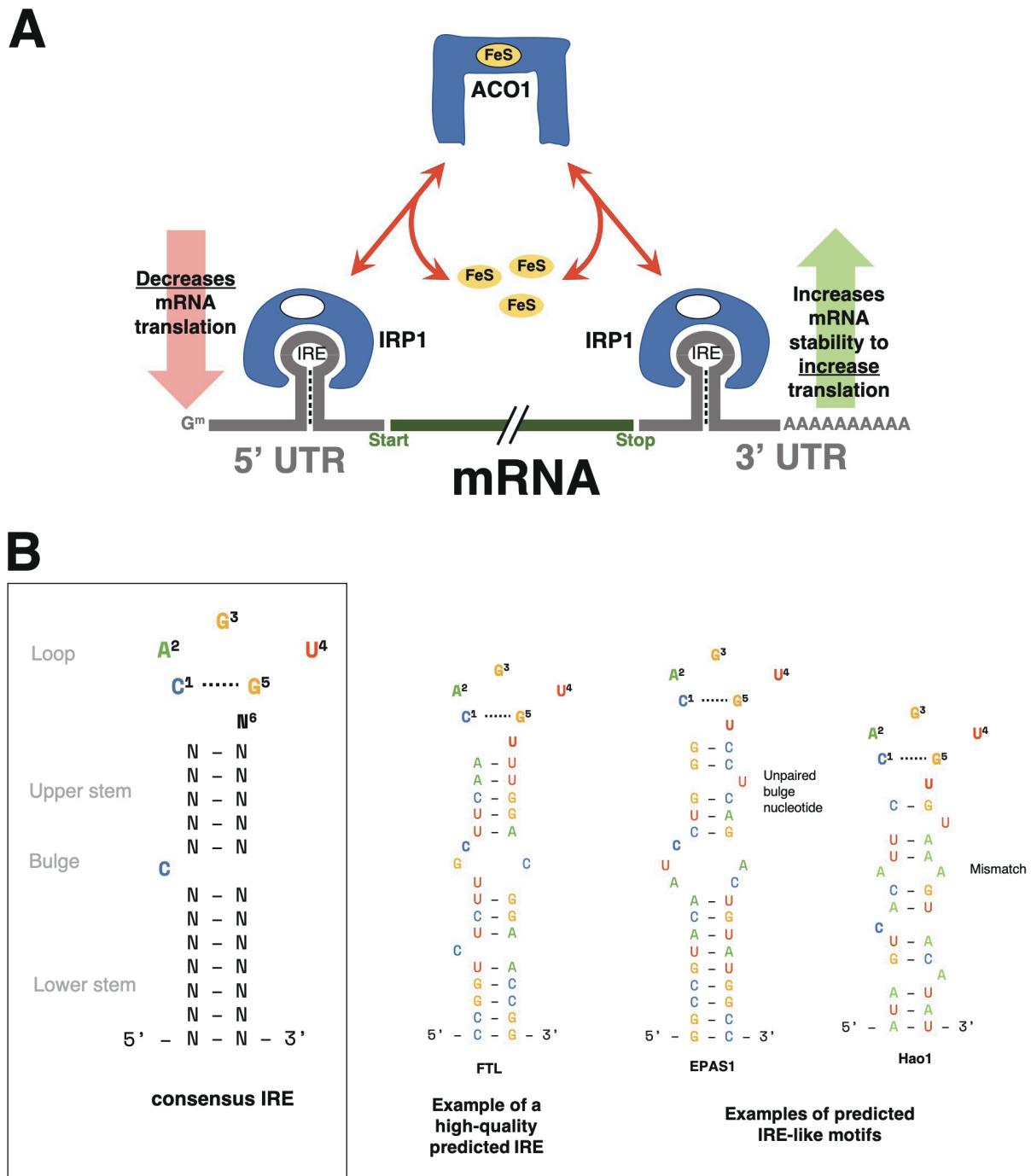
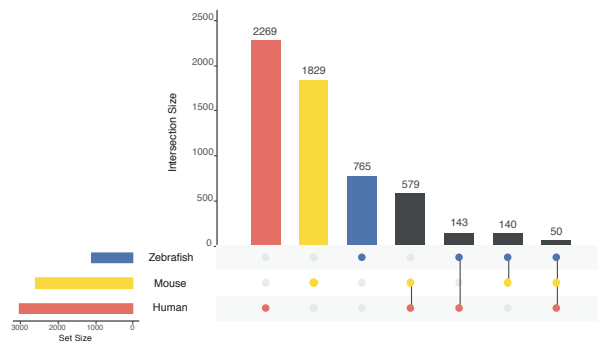
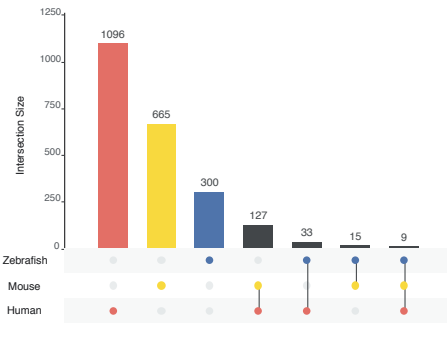


Figure 1. IRE background. A. Model of altered transcript stability due to the IRP/IRE system under iron dyshomeostasis. When cellular iron levels (through FeS) are low, ACO1 will undergo a conformational transformation and act as an IRP to bind IREs in the 5' or 3' untranslated region (UTR) of genes involved in iron homeostasis. In general, genes with IREs in their 3' UTR will be stabilised and increased in expression while genes with IREs in their 5' UTR will have their translation inhibited by the IRP. **B. Consensus IRE secondary structure and examples of high-quality and IRE-like motifs predicted by SIREs.** IRE-like motifs with non-canonical structure are able to be detected by SIREs if they have up to one mismatch pair in the upper stem (e.g. Hao1) or 1 unpaired bulge nucleotide on the 3' strand of the upper stem (e.g. EPAS1). For more details on the prediction of non-canonical IRE motifs, please refer to Figure 1 of Campillos et al. [24].

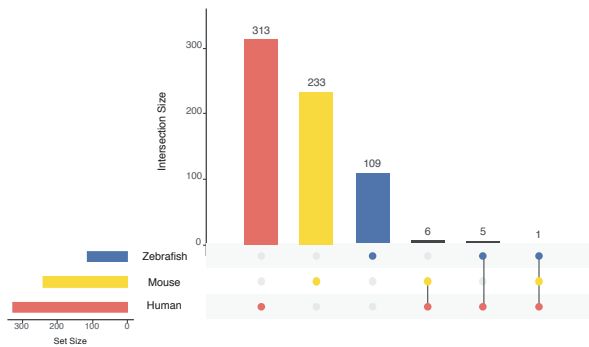
All predicted 3' IRE genes



All predicted 5' IRE genes



High-quality predicted 3' IRE genes



High-quality predicted 5' IRE genes

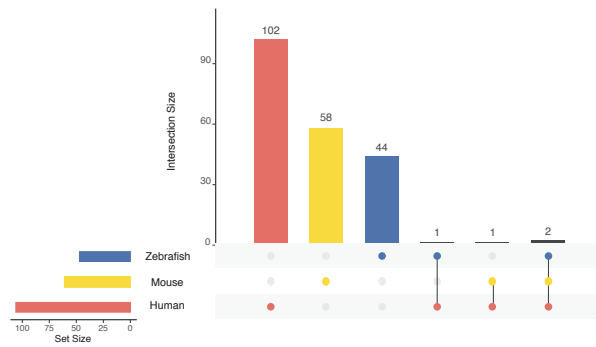
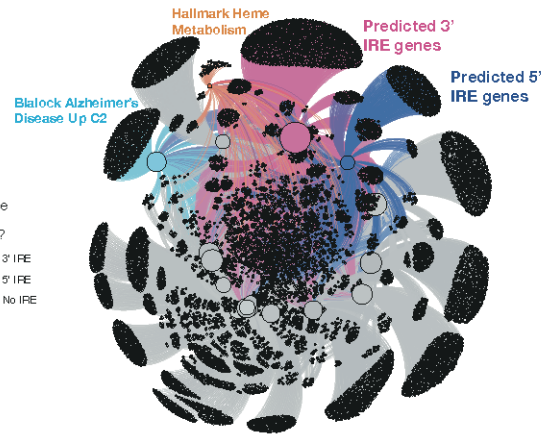
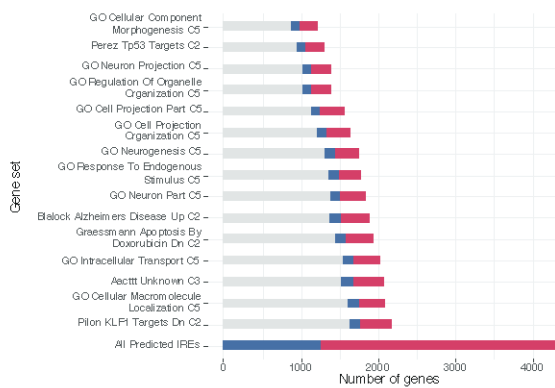
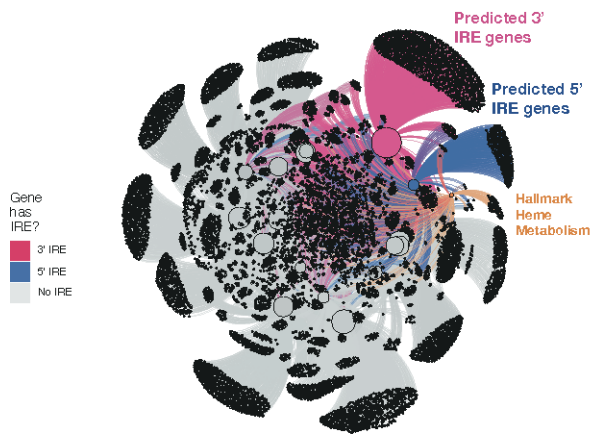
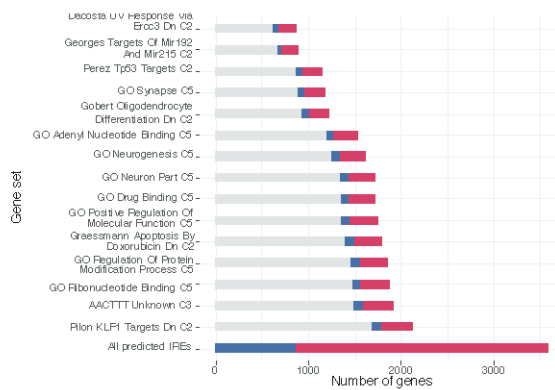


Figure 2. Overlap between predicted IRE gene sets for human, mouse, and zebrafish. The number of genes in the gene set for each species is shown at the bottom-left bars of each UpSet plot, while genes with shared homologs across species are indicated in the main plot region. IRE genes in mouse and zebrafish gene sets were excluded from this plot if they did not have a human homolog.

Human



Mouse



Zebrafish

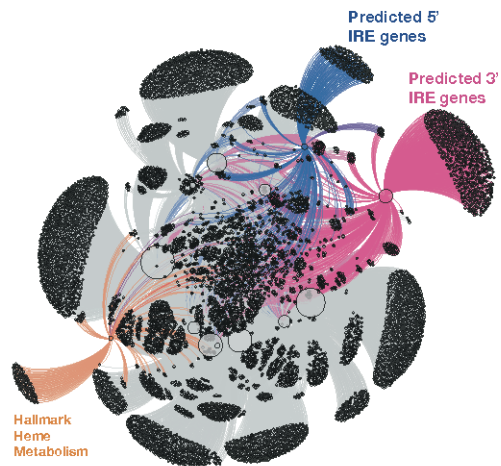
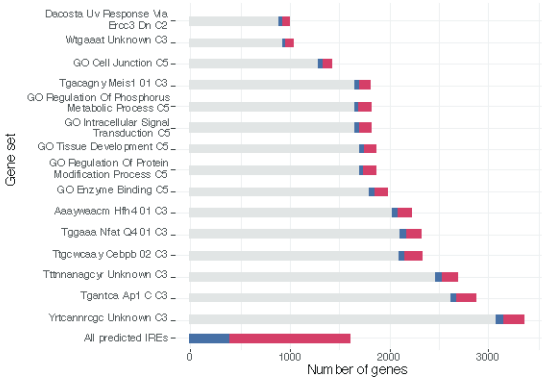


Figure 3. MSigDB gene sets showing over-representation of predicted 3' and 5' IRE genes in human, mouse, and zebrafish. The top 15 MSigDB gene sets ranked by Fisher's exact test p -value (testing for over-representation of the *all 3' IREs* and/or *all 5' IREs* sets) are shown for each species. In the network plots, the top 15 MSigDB gene sets are shown as large nodes, with genes represented as small nodes. Edges connecting genes to gene sets indicate the gene set(s) that a gene belongs to. Overall, the *all 3' IREs* and *all 5' IREs* gene sets have a large proportion of genes which are not included in any of the top ranked MSigDB gene sets for each species.

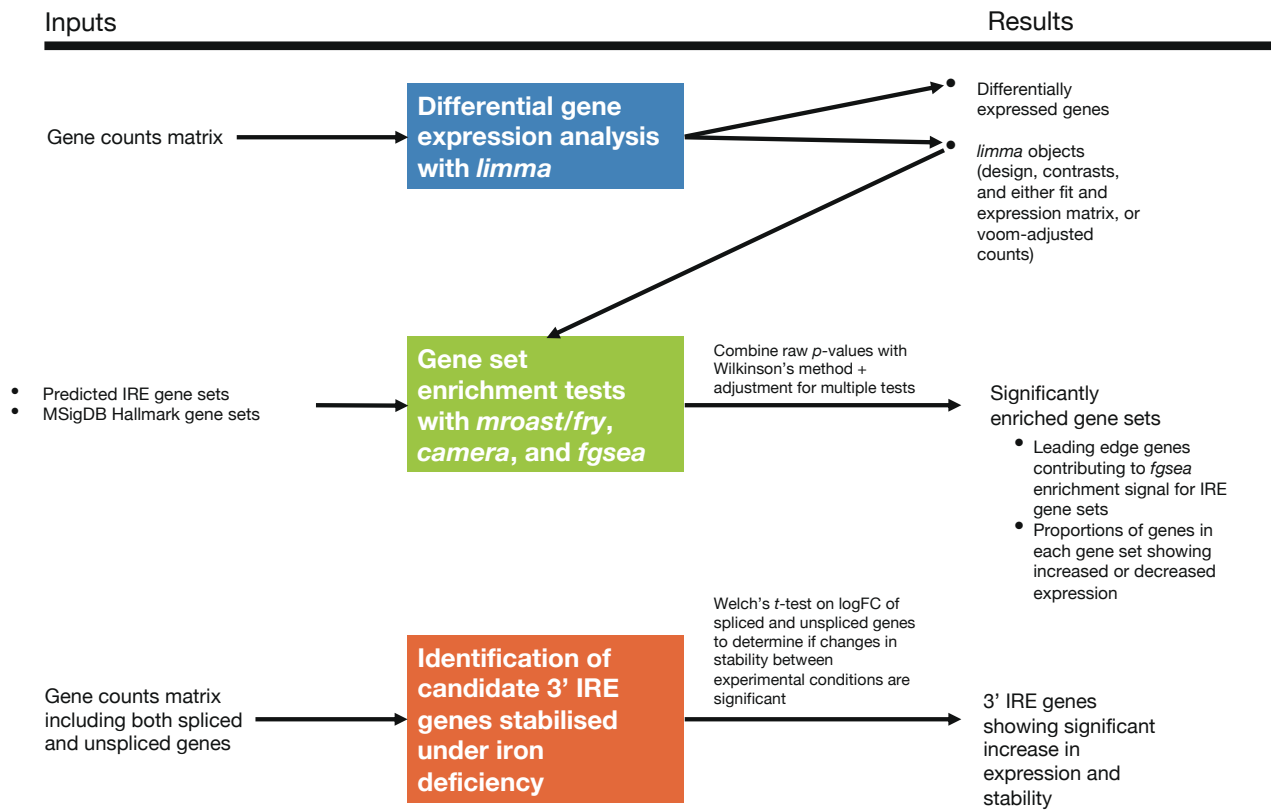


Figure 4. IRE-containing gene expression analysis workflow. The section including identification of candidate 3' IRE genes stabilised under iron deficiency was only applied to the fAD-like zebrafish dataset due to unavailable raw RNA-seq reads for the other datasets needed to identify expression of unspliced genes.

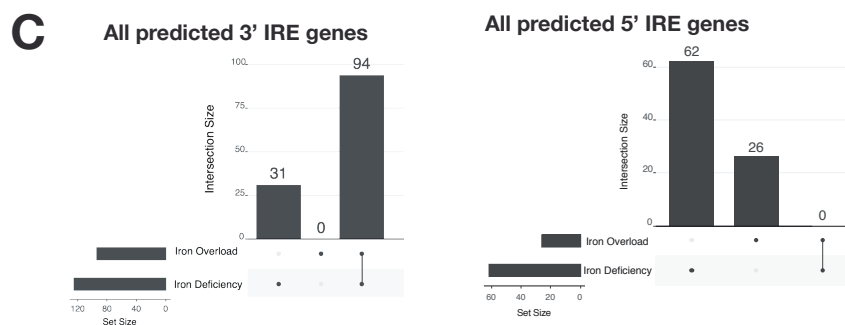
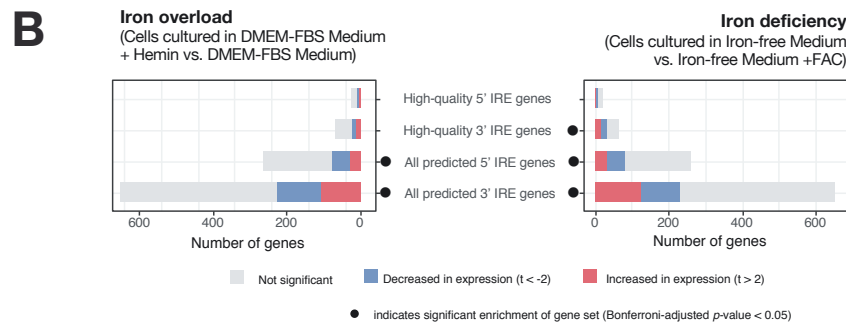
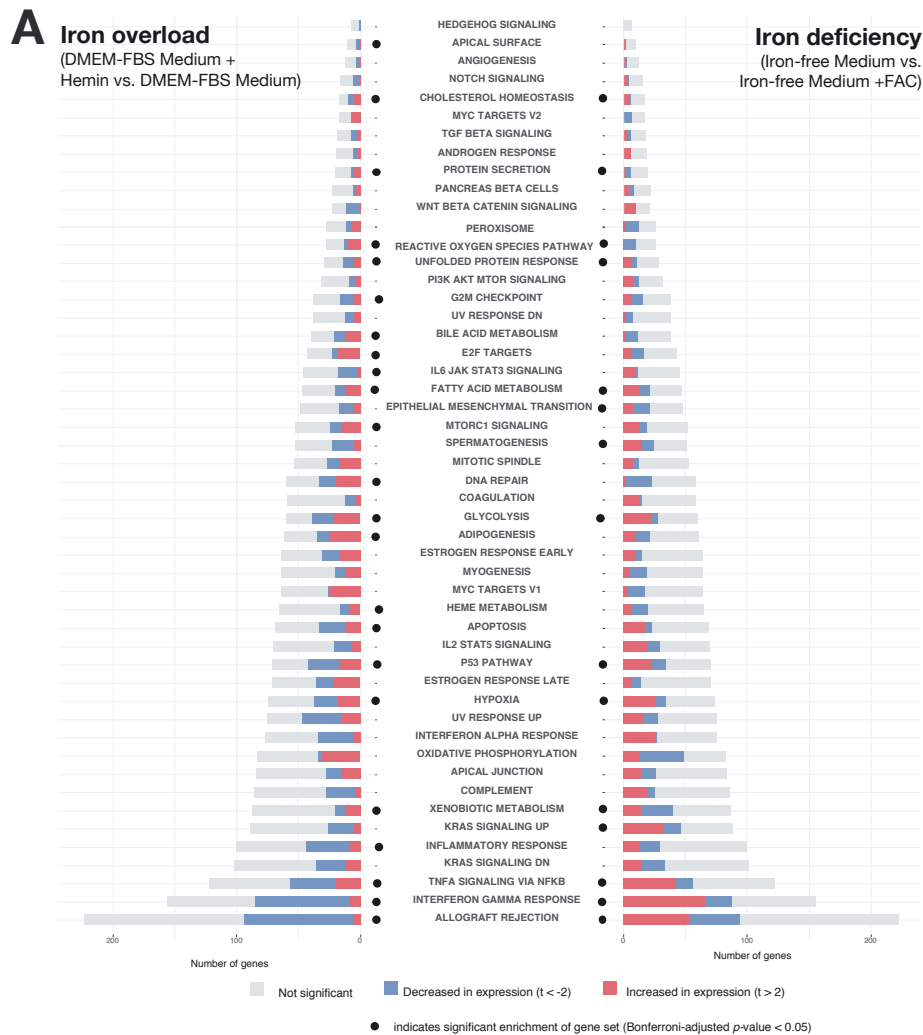
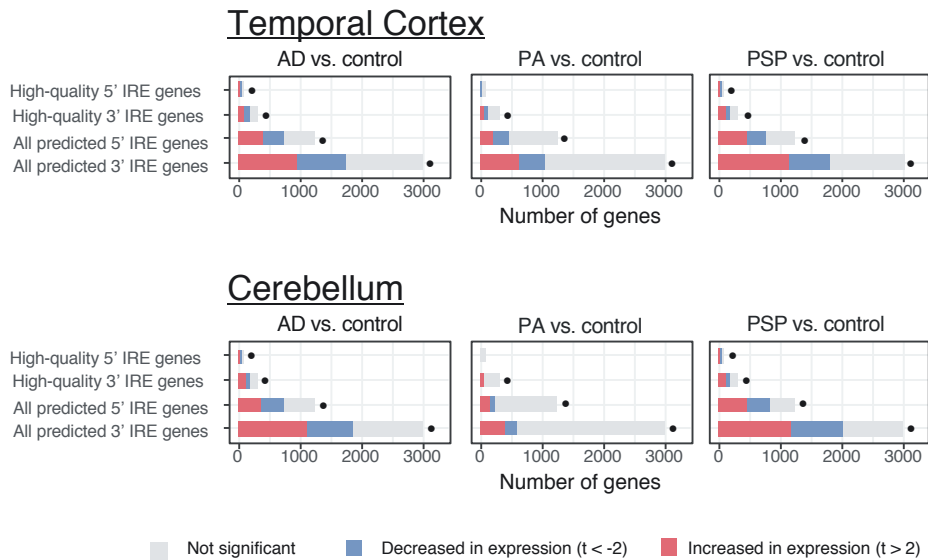


Figure 5. Analysis of Caco-2 cultured cell line microarray dataset. A. Gene set enrichment testing results for human predicted IRE gene sets for the iron overload and iron deficiency treatments. Dots indicate if a gene set was considered significantly enriched (Bonferroni-adjusted p -value < 0.05) in the iron overload (on left) or iron deficiency (on right) treatment. B. Gene set enrichment testing results for MSigDB Hallmark gene sets in the iron overload and iron deficiency treatments. Dots indicate if a gene set was considered significantly enriched (FDR-adjusted p -value < 0.05) in the iron overload (on left) or iron deficiency (on right) treatments. C. UpSet plots showing overlap between iron overload and iron deficiency treatments in GSEA leading-edge genes for the “All predicted 3’ IRE genes” and “All predicted 5’ IRE genes” gene sets. The bars to the lower-left indicate the number of the leading-edge genes for iron overload and iron deficiency treatments, while the bars in the main plot region indicate the number of leading-edge genes which are unique or shared between the treatments.

A

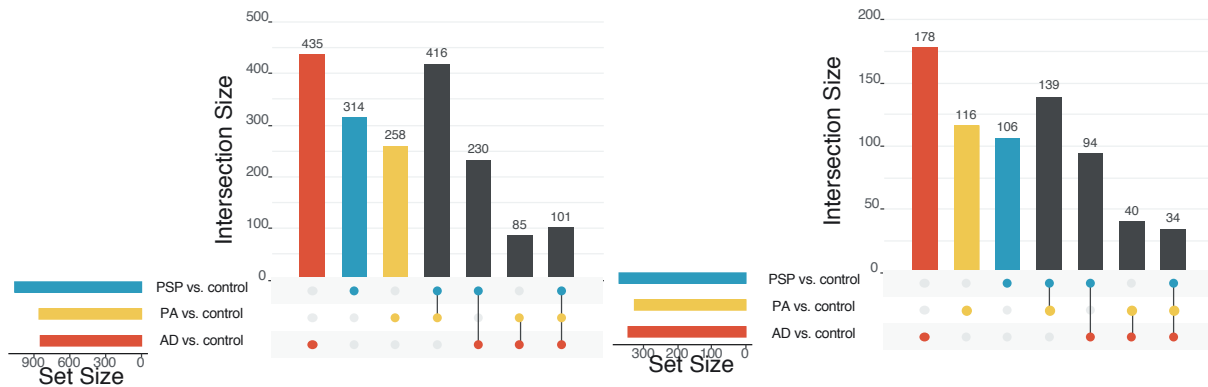


B

Temporal Cortex

Leading-edge genes in all predicted 3' IRE genes

Leading-edge genes in all predicted 5' IRE genes



Cerebellum

Leading-edge genes in all predicted 3' IRE genes

Leading-edge genes in all predicted 5' IRE genes

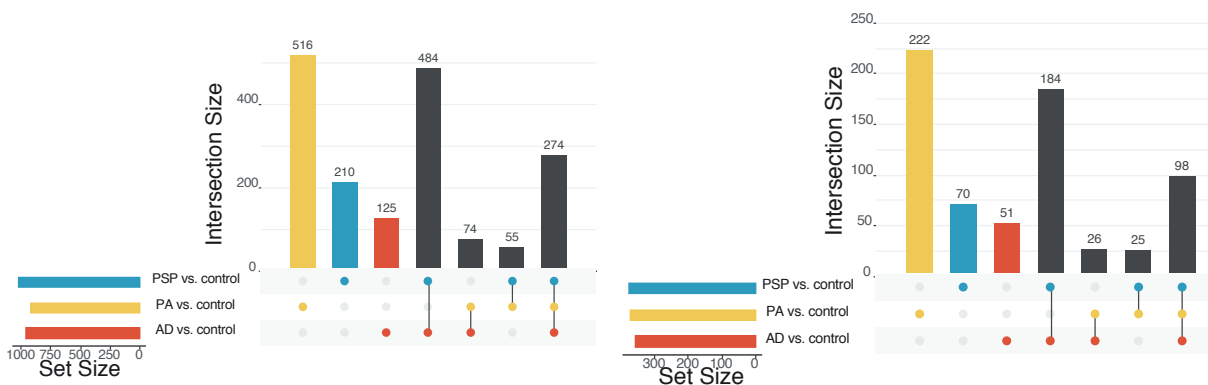


Figure 6. Analysis of Mayo Clinic RNA-seq dataset with human IRE gene sets. A. Enrichment analysis results of IRE gene sets in comparisons of AD (Alzheimer's Disease), PA (Pathological Aging), and PSP (Progressive Supranuclear Palsy) vs. control. The proportions of IRE genes within each IRE gene set with increased, decreased, or unchanged expression are indicated as coloured bars. The dots indicate that the IRE gene set was significantly enriched (Bonferroni-adjusted enrichment p -value < 0.05). B. UpSet plots showing overlap between leading-edge IRE genes in comparisons of AD (Alzheimer's Disease), PA (Pathological Aging), and PSP (Progressive Supranuclear Palsy) vs. control. The bars to the lower-left region of each UpSet plot indicate the number of leading-edge IRE genes for each comparison, while bars in the main plot region indicate the number of leading-edge IRE genes which are unique or shared between comparisons.

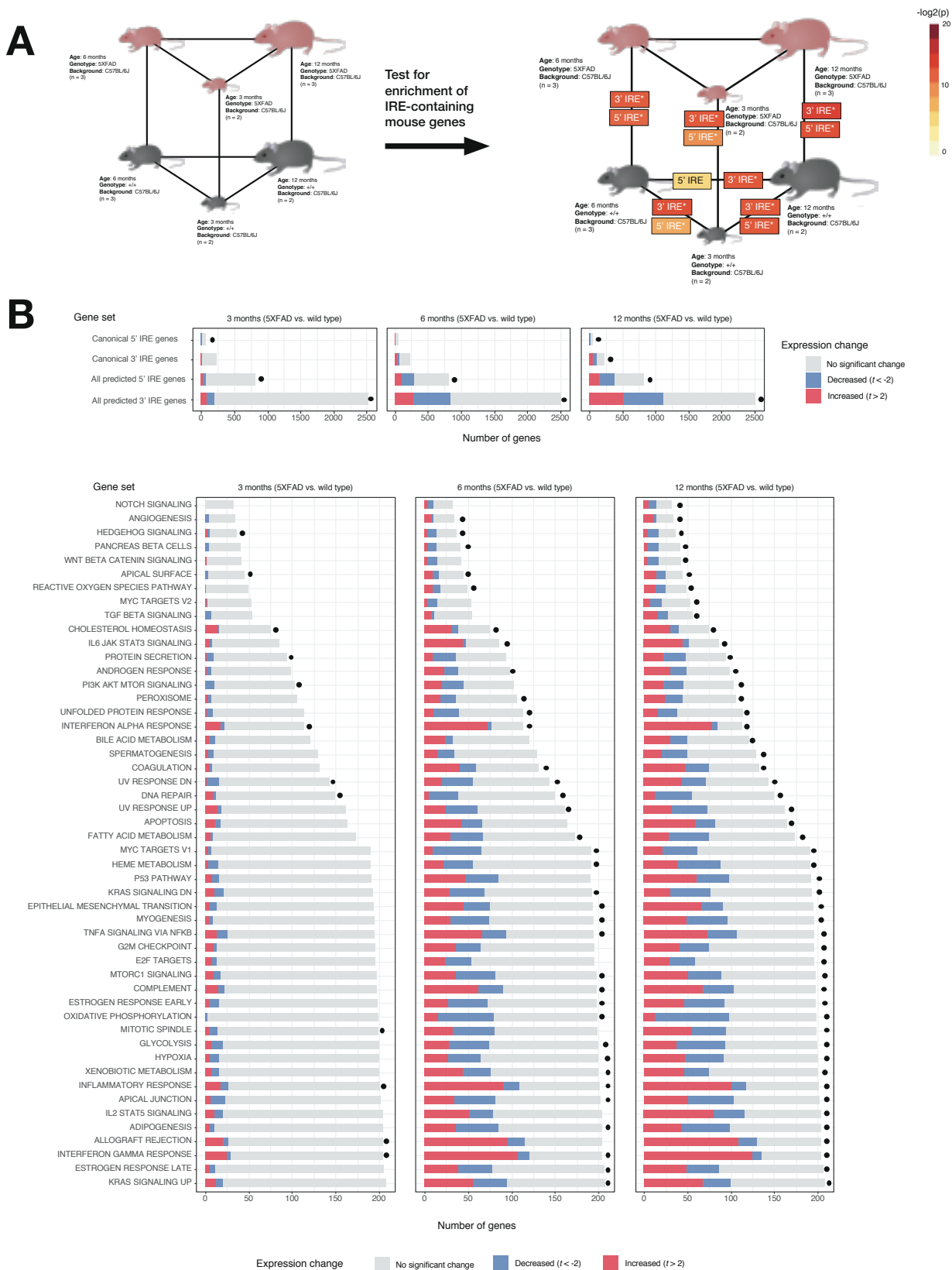


Figure 7. Analysis of 5XFAD mouse dataset. A. Experimental design and results of IRE gene set enrichment analysis. The gene sets *all 3' IREs* and *all 5' IREs* derived from searching for IRE sequences in the UTRs of genes in the reference mouse genome mm10 are represented here as “3' IRE” and “5' IRE” respectively. Asterisks (*) indicate that the gene set was significantly enriched in a particular comparison (Bonferroni-adjusted p -value < 0.05). **B. Proportions of genes in IRE and MSigDB Hallmark gene sets which are increased ($t > 2$) or decreased ($t < -2$) in expression in all “5XFAD vs. wild type” comparisons.** A dot next to a bar indicates that the gene set was significantly enriched (FDR-adjusted p -value < 0.05).

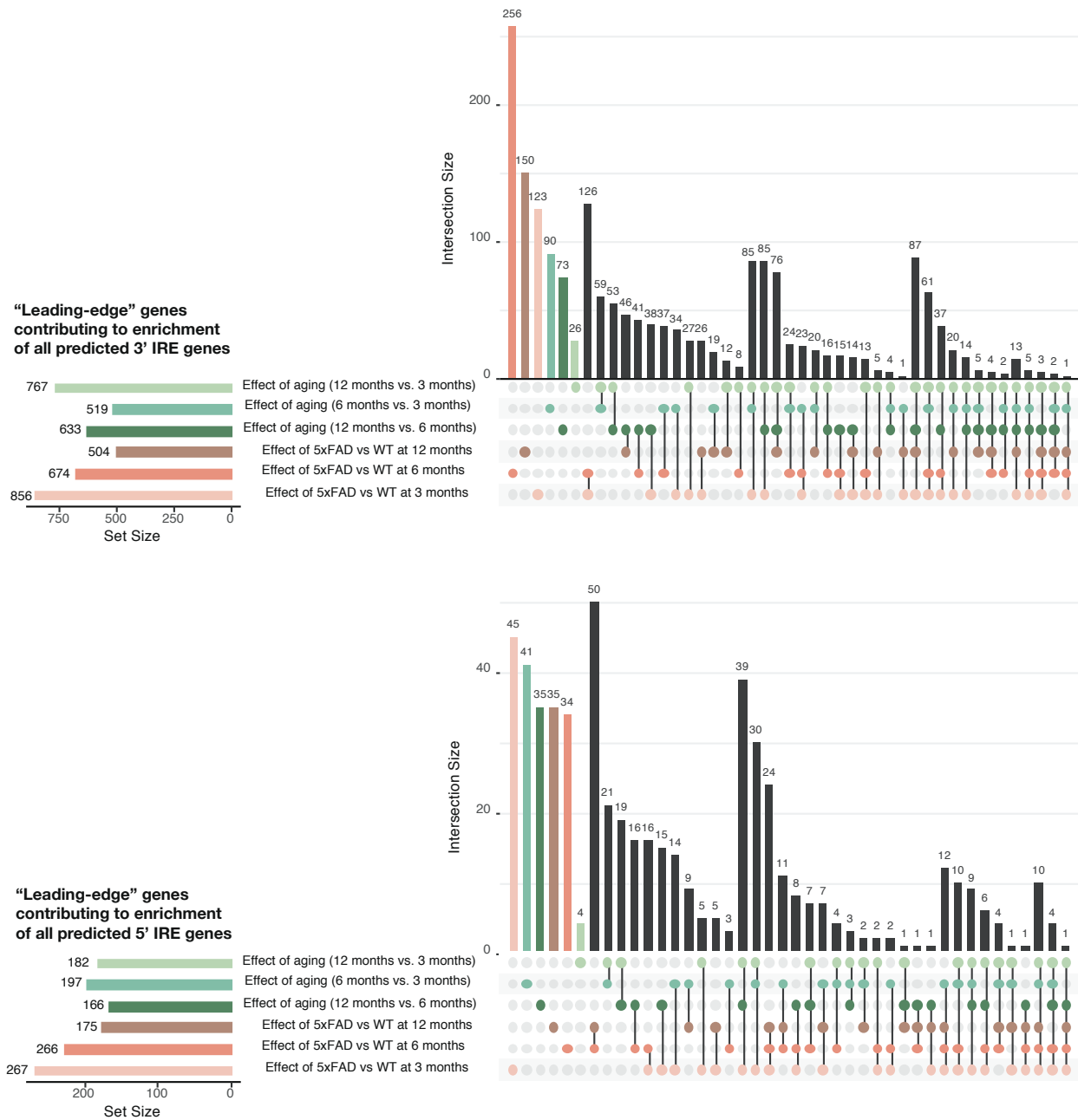


Figure 8. UpSet plots showing the overlap in GSEA leading-edge genes between all comparisons in the 5XFAD mouse datasets for the gene sets *all 3' IREs* and *all 5' IREs*. Numbers of genes for each intersection are shown above intersection bars.

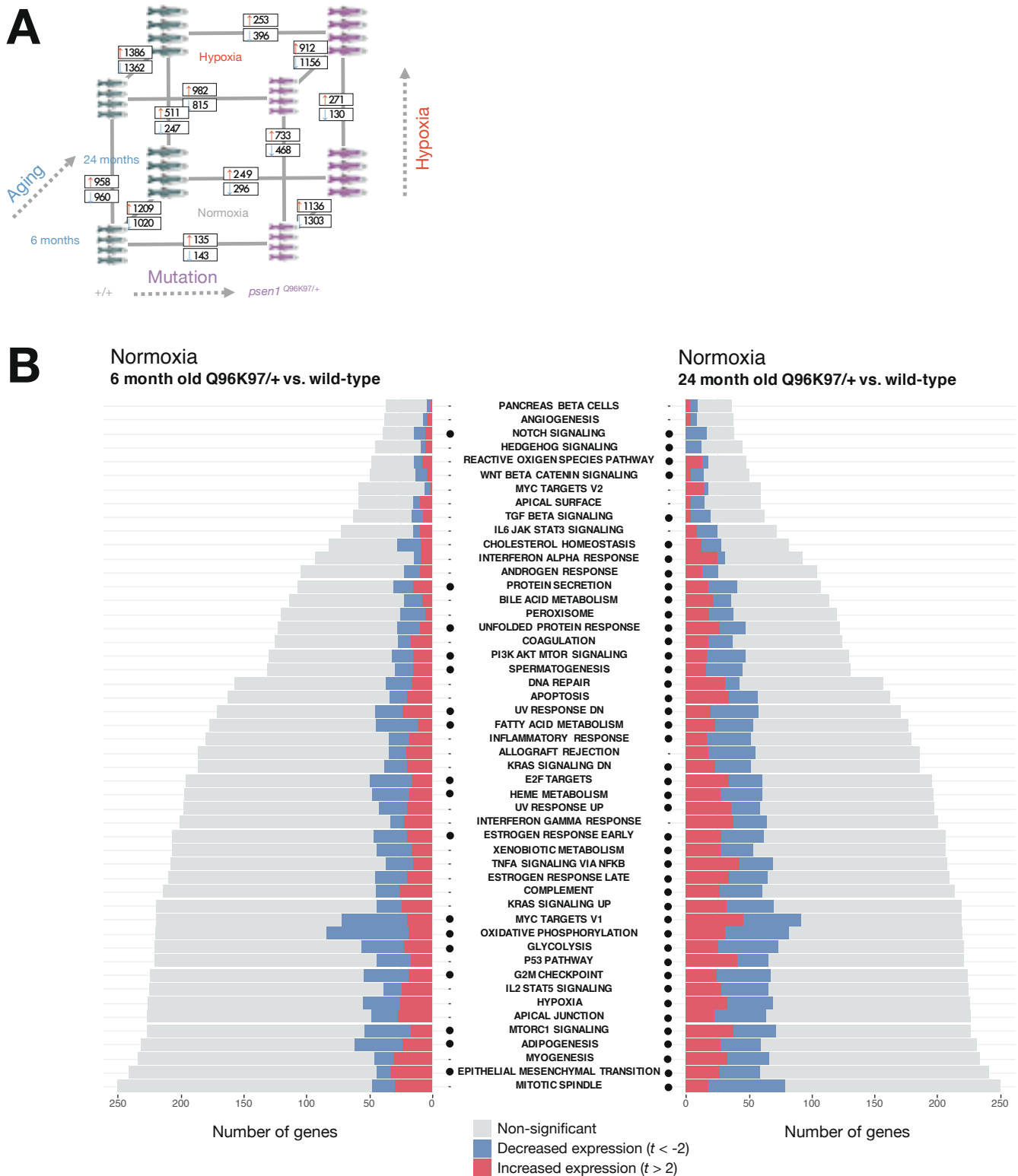


Figure 9. Differential gene expression and gene set enrichment analysis in the fAD-like zebrafish dataset. A. Results of differential gene expression analysis. Genes which were significantly increased or decreased in expression are indicated in boxes. These differentially expressed genes have FDR-adjusted p-value < 0.05 . **B. Gene set enrichment with MSigDB Hallmark gene sets.** The comparisons between Q96_K97del/+ fAD-like mutants and their wild-type siblings are shown for the 6-month-old (young adult) and 24-month-old (infertile adult) age groups. Dots indicate gene sets which are significantly enriched (FDR-adjusted p-value < 0.05).

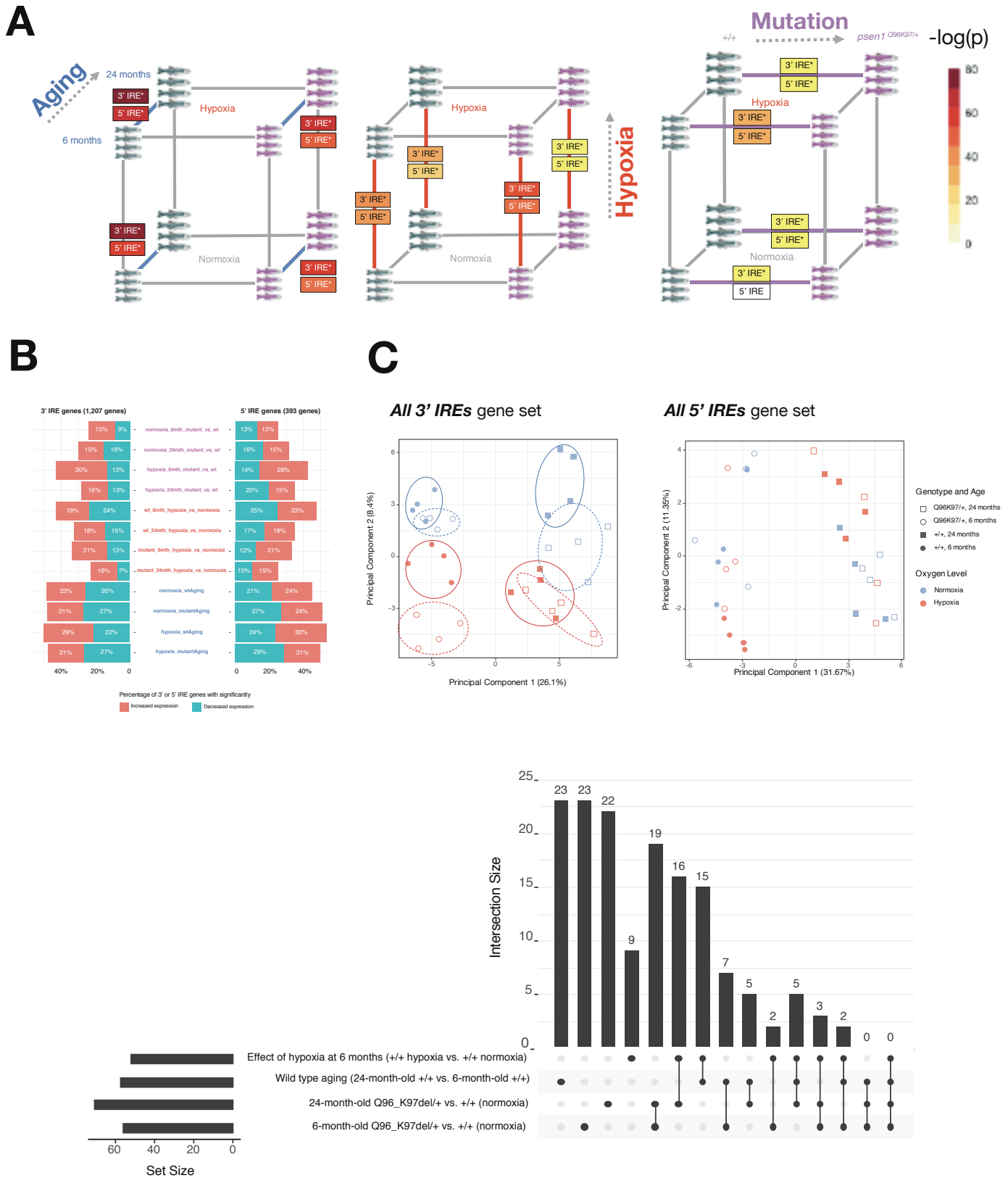


Figure 10. Iron Responsive Element (IRE)-containing gene expression in the fAD-like zebrafish dataset. A. Results of gene set enrichment testing using predicted IRE gene sets. We represent the gene sets *all 3' IREs* and *all 5' IREs* derived from searching for IRE and IRE-like sequences from z11 reference zebrafish gene UTRs as “3' IRE” and “5' IRE” in the panel. B. Proportions of predicted IRE genes which are increased ($t > 2$) or decreased ($t < -2$) in expression for each pairwise comparison in the dataset. C. Principal component analysis of all genes in the sets *all 3' IREs* and *all 5' IREs* for all samples. Circles on the 3' IRE plot show that different conditions generally have distinct expression of genes in the *all 3' IREs* set but not in the *all 5' IREs* set. D. UpSet plot showing overlap in leading-edge genes for the “all predicted 3' IRE genes” for select comparisons.

Tables

Table 1. Summary of gene set testing approaches used in our analyses.

Method	Hypothesis	Focused / battery approach	Accounts for inter-gene correlation	R implementation
Fry / Roast	Self-contained null hypothesis (genes within a set have no association with experimental condition)	Focused (each gene set is tested on its own terms, and multiple testing adjustment is applied afterwards)	Yes	fry() and mroast() functions in the <i>limma</i> Bioconductor package (Wu et al. 2010)
Camera	Competitive null hypothesis (genes within a set do not have a stronger association with experimental condition compared to a random gene set)	Focused (each gene set is tested on its own terms, and multiple testing adjustment is applied afterwards)	Yes	camera() function in the <i>limma</i> Bioconductor package (Wu & Smyth 2012)
fgsea (fast implementation of GSEA in R)	Self-contained null hypothesis (genes within a set have no association with experimental condition)	Battery (gene sets are pitted against each other to determine which ones are more significantly enriched)	No	fgsea() function in the <i>fgsea</i> Bioconductor package (Subramanian et al. 2005)

Table 2. Samples analysed from Mayo Clinic RNA-seq study.

Group	Total number	% Female	Mean age \pm s.d (years)	Diagnosis
Alzheimer's disease (AD)	134	56.7	82.6 \pm 7.3	Braak Stage \geq 4, diagnosis according to NINCDS-ADRDA criteria
Control	130	46.2	82.9 \pm 8.3	Braak Stage \leq 3, No or sparse CERAD neuritic and cortical plaque density, no diagnoses for any neurodegenerative disease
Pathological Aging (PA)	44	54.5	84.5 \pm 4.3	Braak Stage \leq 3, CERAD neuritic and cortical plaque density of 2 or more, no diagnoses for any neurodegenerative disease or mild cognitive impairment
Progressive supranuclear palsy (PSP)	164	40.2	73.8 \pm 6.5	Braak Stage \leq 3, no or sparse CERAD neuritic and cortical plaque density

Table 3. Differential gene expression and IRE gene set enrichment results from Mayo Clinic RNA-seq study. Shaded cells indicate significant enrichment (Bonferroni-adjusted Wilkison's p -value from *fry*, *camera*, and *fgsea* < 0.05).

	Comparison	No. of DE genes (FDR p -value < 0.05 and $\text{abs}(\log\text{FC}) > 0.5$)	All predicted 3' IRE gene enrichment p - value	All predicted 5' IRE gene enrichment p - value	Canonical 3' IRE gene enrichment p - value	Canonical 5' IRE gene enrichment p - value
Effect of Alzheimer's disease	AD vs. control (cerebellum)	Down: 1,422 Up: 1,308	0.0109	0.128	0.770	0.770
	AD vs. control (temporal cortex)	Down: 1,650, Up: 1,929	9.03E-15	2.44E-14	4.50E-15	8.95E-08
Effect of pathological aging (amyloid pathology, no dementia symptoms)	PA vs. control (cerebellum)	Down: 254, Up: 463	0.000116	0.00139	0.0201	0.770
	PA vs. control (temporal cortex)	Down: 466, Up: 512	0.000521	0.0461	0.000065	0.0000682
Effect of progressive supranuclear palsy (PSP)	PSP vs. control (cerebellum)	Down: 2,550, Up: 1,080	1.81E-22	3.45E-22	1.43E-12	0.0399
	PSP vs. control (temporal cortex)	Down: 1,271, Up: 622	3.58E-11	5.17E-13	1.39E-06	0.0399
Differences between Alzheimer's disease and pathological aging	AD vs. PA (cerebellum)	Down: 1,728, Up: 1,006	0.000116	0.00139	0.0201	0.770
	AD vs. PA (temporal cortex)	Down: 2,633, Up: 2,174	0.000521	0.0461	0.000065	0.0000682
Differences between Alzheimer's disease and progressive supranuclear palsy	AD vs. PSP (cerebellum)	Down: 108, Up: 659	0.0019	0.00184	0.158	0.158
	AD vs. PSP (temporal cortex)	Down: 2,052, Up: 2,354	9.12E-22	2.10E-22	5.35E-16	0.040
Differences between cerebellum and temporal cortex tissue	Cerebellum vs. temporal cortex in controls	Down: 10,925, Up: 9,302	0.00E+00	0.00E+00	2.82E-269	1.60E-81
	Cerebellum vs. temporal cortex in AD	Down: 11,966, Up: 9,950	0.00E+00	0.00E+00	7.71E-302	9.35E-92
	Cerebellum vs. temporal cortex in PA	Down: 10,200, Up: 8,737	1.87E-153	5.88E-160	1.22E-89	1.31E-88
	Cerebellum vs. temporal cortex in PSP	Down: 11,552, Up: 9,576	0.00E+00	0.00E+00	0.00E+00	4.74E-104

Table 4. Enrichment of Iron Responsive Element (IRE) gene sets in fAD-like zebrafish dataset. Raw *p*-values from *fry*, *camera* and *fgsea* were combined with Wilkinson's method, with combined *p*-values then Bonferroni-adjusted for multiple testing. The same process was repeated for the K97fs/+ dataset, which involves an independent family of fish (shaded cells).

	Comparison	All predicted 3' IRE gene enrichment <i>p</i> -value	All predicted 5' IRE gene enrichment <i>p</i> -value	Canonical 3' IRE gene enrichment <i>p</i> -value	Canonical 5' IRE gene enrichment <i>p</i> -value
Effect of <i>psen1</i> mutation	6-month-old Q96_K97del/+ vs. 6-month-old +/+ all under normoxia	0.0109	0.128	0.770	0.770
	6-month-old Q96_K97del/+ vs. 6-month-old +/+ all under hypoxia	9.03E-15	2.44E-14	4.50E-15	8.95E-08
	24-month-old Q96_K97del/+ vs. 24-month-old +/+ all under normoxia	0.000116	0.00139	0.0201	0.770
	24-month-old Q96_K97del/+ vs. 24-month-old +/+ all under hypoxia	0.000521	0.0461	0.000065	0.0000682
	6-month-old K97fs/+ vs. 6-month-old +/+ all under normoxia	0.199	0.289	0.0197	0.289
	24-month-old K97fs/+ vs. 24-month-old +/+ all under normoxia	0.116	0.115	0.00000118	0.979
	6-month-old +/+ under hypoxia vs. 6-month-old +/+ under normoxia	1.10E-18	1.10E-18	8.19E-13	1.27E-08
Effect of hypoxia	24-month-old +/+ under hypoxia vs. 24-month-old +/+ under normoxia	3.67E-15	7.98E-11	2.94E-07	3.31E-05
	6-month-old Q96_K97del/+ under hypoxia vs. 6-month-old Q96_K97del/+ under normoxia	1.13E-24	9.88E-22	2.28E-13	2.86e-3
	24-month-old Q96_K97del/+ under hypoxia vs. 24-month-old Q96_K97del/+ under normoxia	0.000521	0.015	0.128	0.770
	24-month-old +/+ vs. 6-month-old +/+ all under normoxia	6.80E-35	4.82E-27	3.41E-18	1.26E-21
Effect of aging	24-month-old +/+ vs. 6-month-old +/+ all under hypoxia	1.55E-35	6.84E-31	2.36E-20	7.40E-23
	24-month-old Q96_K97del/+ vs. 6-month-old Q96_K97del/+ all under normoxia	1.85E-27	1.03E-21	8.09E-17	1.07E-17
	24-month-old Q96_K97del/+ vs. 6-month-old Q96_K97del/+ all under hypoxia	3.77E-30	1.59E-23	2.11E-19	2.46E-16
	24-month-old +/+ vs. 6-month-old +/+ all under normoxia (K97fs family)	1.69E-10	3.96E-08	5.95E-10	4.59E-06
	24-month-old K97fs/+ vs. 6-month-old K97fs/+ all under normoxia	0.199	0.289	0.0197	0.289